Applied Mathematical Modelling 99 (2021) 760–784

Contents lists available at ScienceDirect

Applied Mathematical Modelling

journal homepage: www.elsevier.com/locate/apm

Numerical modelling of interaction between aluminium structure and explosion in soil

Jian-Yu Chen[a], Dian-Lei Feng[b], Fue-Sang Lien[c], Eugene Yee[c], Shu-Xin Deng[a], Fei Gao[a], Chong Peng[d,*]

[a] School of Mechanical Engineering, Nanjing University of Science and Technology, 200 Xiaolingwei Street, Xuanwu District, Nanjing, 210094, China
[b] Institute of Fluid Mechanics and Environmental Physics in Civil Engineering, Leibniz University Hannover, Appelstraße 9A Hannover 30167, Germany
[c] Department of Mechanical and Mechatronics Engineering, University of Waterloo, 200 University Avenue West, Waterloo, Ontario, N2L 3G1, Canada
[d] Institut für Geotechnik, Universität für Bodenkultur, Feistmantelstrasse 4, Vienna 1180, Austria

ARTICLE INFO

Article history:
Received 12 February 2021
Revised 8 July 2021
Accepted 10 July 2021
Available online 18 July 2021

Keywords:
Explosive detonation in soil
Smoothed particle hydrodynamics
Graphics processing unit acceleration
Aluminium plate damage

ABSTRACT

In this paper, a graphics processing unit-accelerated smoothed particle hydrodynamics solver is presented to simulate the three-dimensional explosions in soils and their damage to aluminium structures. To achieve this objective, a number of equations of state and constitutive models required to close the governing equations are incorporated into the proposed smoothed particle hydrodynamics framework, including the Jones-Wilkins-Lee equation of state for explosive materials, the Grüneisen equation of state for metals, the elastic-perfectly plastic constitutive model for metals, and the elastoplastic and elasto-viscoplastic constitutive models for soils. The proposed smoothed particle hydrodynamics methodology was implemented using the Compute Unified Device Architecture programming interface on an NVIDIA graphics processing unit in order to improve the computational efficiency. The various components of the proposed methodology were validated using four test cases, namely, a C4 detonation and an aluminium bar expanded by denotation to validate the modelling of explosion, a cylindrical Taylor bar impact test case to validate the modelling of large deformation in metals, a sand collapse test for the modelling of soils. Following the validation, the proposed method was used to simulate the detonation of an explosive material (C4) in soil and the concomitant deformation of an aluminium plate resulting from this explosion. The predicted results of this simulation are shown to be in good conformance with available experimental data. Finally, it is shown that the proposed graphics processing unit-accelerated SPH solver is able to model interaction problems involving millions of particles in a reasonable time.

* Corresponding author.
E-mail addresses: chenjianyu@njust.edu.cn (J.-Y. Chen), pengchong@boku.ac.at (C. Peng).

https://doi.org/10.1016/j.apm.2021.07.010

1. Introduction

Landmines and shallow-buried improvised explosive devices (IEDs) are some of the dangers in zones of conflict that armoured vehicles and personnel must contend with. Such a device is typically activated and detonated when a target drives over it or steps on it, which can potentially cause severe damage to the vehicle or person through either direct blast effects or by the fragmentation of soil and concomitant soil ejecta that are generated by blast. In consequence, the prediction of the detonation of an explosive device buried in soil and the resulting damage to metal structures in its vicinity is a problem of significant importance in civil engineering and military defence.

Various approaches that have been used for the investigation of the detonation of an explosive device in soil and the concomitant damage to nearby metal structures have ranged from experimentation to simulation. For example, Rigby et al [1] used a purely experimental approach to address this problem, involving the direct measurement of the spatial and temporal variation of the pressure distribution resulting from an explosive detonation in dry sand. Linforth et al [2] conducted both experimental and numerical investigations of the blast loading generated by an explosive charge buried in an unsaturated soil. Resnyansky and Weckert [3] developed a test platform of porous materials with a planar shock impact and split Hopkinson pressure bar and used this platform to investigate the dynamic response of geological porous materials to loading from an explosive detonation. In spite of this effort, the use of experimentation to study the phenomenology of an explosion in granular media (soil) is rather restricted owing to its prohibitive cost and difficulties in measurement of physical phenomena occurring on very short time scales. In consequence, the numerical simulation is an alternative methodology that has been applied to study the myriad and complex physical processes involved in an explosive detonation in soil and concomitant damage to engineering structures located in the vicinity of the explosion.

Conventional mesh-based methods such as the finite difference method (FDM), finite element method (FEM), and finite volume method (FVM) have been widely used to address various geomechanics problems. However, the large deformations that characterize an explosive detonation in soil can result in significant distortions in the mesh when applying these conventional mesh-based methods to the problem. As a result, these distortions can result in numerical instabilities in the simulation which can lead to a pre-mature termination of the calculations. In view of these difficulties, we use instead the smoothed particle hydrodynamics (SPH) methodology to predict the detonation of explosive devices in soil and their interaction with metal structures, which involve complex multi-phase and multi-physics processes.

There are significant advantages in using the SPH methodology to address this problem. Firstly, a mesh-free particle method such as SPH bridges the gap between the continuum modeling and discrete modeling of granular materials. In particular, granular materials can behave as a solid for which continuum models are appropriate but also as a gas-like disconnected state resulting from fragmentation of the granular materials as a result of an explosive detonation for which discrete models are necessary. SPH provides a natural unified numerical and modeling framework for addressing this issue. Secondly, the SPH methodology addresses complex material interfaces involving materials with significantly different properties in a simpler and more natural manner than mesh-based numerical methods such as FDM or FEM [4].

The SPH methodology was independently proposed by Gingold and Monaghan [5] and by Lucy [6]. The methodology was originally used for numerical simulation of various astrophysical phenomena (e.g., galaxy dynamics, star formation, stellar collisions). SPH is a mesh-free particle-based simulation for fluids which is built on solving discretized forms of the Lagrangian conservation equations of fluid dynamics. Owing to its mesh-free Lagrangian nature, the applications of the SPH methodology have been extended to problems involving large deformations such as free surface flows, explosive detonation, and geomechanics problems. Liu et al [7] simulated a one-dimensional TNT slab detonation and a two-dimensional (2D) underwater explosion using the SPH methodology. This study demonstrated that both the magnitude and location of the shock wave arising from an underwater explosion can be well modeled using SPH. Wang et al [8] implemented a reactive flow model and applied this model within a SPH framework to simulate a three-dimensional (3D) non-ideal explosive detonation of ammonium nitrate/fuel oil (ANFO). Feng et al [9] investigated the jet formation generated by the detonation of a linear-shaped charge as well as the penetration of this charge into a metal structure. Fan and Li [10] implemented several geomaterial models within a coupled peridynamics-SPH methodology and used this framework to simulate 3D soil fragmentation resulting from a buried explosive load. The peridynamics-SPH methodology proposed in this work accounts properly for the porosity and viscoplasticity of the soil and for the effects of strain softening and provided generally good agreement between the numerical predictions and some available experimental data related to 3D soil explosion. Chen and colleagues [11–13] used the SPH methodology to investigate 2D and 3D soil explosion and 3D underwater explosion problems. Furthermore, an elasto-viscoplastic constitutive model is used to investigate the 3D flow dynamics of granular materials using SPH [14].

In spite of the fact that simulations of soil explosion have been conducted by numerous researchers, the prediction of the detonation of an explosive device in soil and the determination of the damage incurred by nearby metal structures has not been adequately addressed to date due to the following reasons: firstly, the explosion in soil involves extremely large deformations, which may provoke mesh distortion or even computational termination in simulations when using conventional mesh-based methods. Although some advanced FEM-based methods with constant remeshing are developed to model problems with large deformation, the modelling of explosion in soil is still challenging. Secondly, the explosion in soil is a complex multi-phase problem with very large density ratio between the explosive gaseous products and the soil, which may lead to numerical instability. Although SPH is commonly used to model problems with large deformation and free-surface flows, the numerical simulation of 3D soil explosion and its damage to metal structures cannot be tackled by the standard

SPH method. Thus, special treatment is required for the large density ratio within SPH. Thirdly, SPH is a computationally intensive method, the simulation of 3D explosion problems, which needs millions of particles to achieve satisfactory accuracy, is beyond the capability of serial computing or parallel computing with limited number of CPU cores. In view of this, the primary objective of the current research is to develop a general SPH methodology that can be used to address this important problem.

The applicability of a mesh-free particle-based SPH methodology is generally limited by two computational constraints; namely system size and computational time. To be able to obtain physically relevant information from a SPH simulation, it is critically important to be able to simulate a large enough system for a long enough time (viz., it is necessary to simulate the collective motions of millions to tens of millions of particles over a long-enough time of physical relevance in a reasonable time on the computational platform). To this purpose, SPH has taken advantage of the parallelism inherent in graphics processing units (GPUs) in order to improve the computational efficiency of a SPH simulation. Mokos et al [15] applied GPU accelerators for the multi-phase modeling of violent hydrodynamics. These investigators demonstrated that their implementation of the SPH methodology on a single GPU gave a speed-up of two orders of magnitude when benchmarked against an optimized CPU SPH code. Peng et al [16] developed an open-source GPU-accelerated SPH solver for soil modeling. Numerical simulations conducted using this solver (referred to as LOQUAT) showed that it is efficient in modeling problems such granular flows and large deformations in soils. Recently, other researchers also reported speed-up more than two orders of magnitude when comparing GPU and serial CPU SPH computing with high-end hardware [17,18]. Following on from these efforts, we have implemented our SPH methodology for addressing problems involving soil explosion and concomitant damage to nearby metal structures with the Compute Unified Device Architecture (CUDA) programming interface for single GPUs. As reported later in the paper, this has resulted in a high-performance and scalable SPH simulation code that enables us to conduct simulations of this important problem using high-resolution models in a reasonable (wall-clock) time.

Our group developed the SPH methodology to investigate the processes of explosion in soil [11,12], underwater explosion [13], and the dynamics behavior of granular media [14,19]. The methodology used in this study is different from our previous research. In the previous studies, the Monaghan-type boundary treatment method, CPU-based tree search algorithm, leapfrog integration, and Open-MP parallel computing platform were employed. The number of particles in the simulation of explosion in soil is limited to 1.15 million, and even with that limited number of particles, the simulation time is already 72 hours [12] when using Intel E5- 2683 CPU. It is known that more accurate numerical results (e.g., peak pressure and height of soil fragmentation) can be obtained with more particles (see Fig. 12 in [11] and Fig. 11 in [13]). However, further increasing the particle number is impossible with the previous methodology. On the other hand, the newly developed GPU-accelerated SPH methodology with Adami-type boundary treatment method, modified linked-list search algorithm, and predictor-corrector time integration method are employed in the current research. Much more particles can be used in the simulations, so that the shock wave propagation can be better predicted. Secondly, this work is probably the first 3D simulation of damage of aluminium plates incurred by soil explosions. The large deformation and failure pattern of the metal plate obtained from SPH are compared with experimental data. Furthermore, an elasto-viscoplastic model has been included to investigate its performance in modelling high-speed impacts. In comparison with other research, such as Fan et al. [10], the soil explosion has been simulated using a pure SPH method instead of methods such as FEM or the peridynamics-SPH coupled method. We make full use of the meshfree and Lagrangian nature of SPH, and forge a method with simple formulation, easy implementation, high efficiency, and satisfactory accuracy. The complex mesh treatment in FEM and peridynamics-SPH coupling algorithm are avoided.

This paper is organized into eight sections. Section 2 is a brief introduction to the fundamental concepts underpinning the SPH methodology. Section 3 describes the equations of state and constitutive models used in our SPH simulations of explosive detonation in soil and assessment of the damage incurred by nearby metal structures. Section 4 provides a brief description of the implementation of the proposed SPH methodology on a GPU. The various components of the GPU-accelerated SPH methodology are validated in Section 5 using four benchmark test cases. Following from this systematic validation effort, we apply the proposed SPH methodology to model the detonation of an explosive device in soil in Section 6. Section 7 presents an investigation of the damage of the 3D soil explosion to an aluminium (Al) plate located in the vicinity of the detonation. Key conclusions of this study and future work are summarized in Section 8.

2. Fundamentals of the SPH methodology

2.1. Function approximation in SPH

In the SPH methodology, the hydrodynamic equations in Lagrangian form are discretized into a set of particles whose properties change as the (simulated) fluid moves. More specifically, the positions of the SPH particles define the properties of the fluid throughout the flow through an interpolation technique. The continuous SPH approximation of a fluid property $f(\boldsymbol{x})$ as a function of the spatial coordinates $\boldsymbol{x}$ is obtained using the following integral interpolant:

$$\langle f(\boldsymbol{x})\rangle = \int_{\Omega} f(\boldsymbol{x}')W(\boldsymbol{x}-\boldsymbol{x}', h)d\boldsymbol{x}',$$

where W is the weight or kernel function, h is the smoothing length, and Ω is the computational domain. When the kernel function converges to the Dirac delta function (viz., $\lim_{h\to 0} W(\boldsymbol{x}-\boldsymbol{x}', h) = \delta(\boldsymbol{x}-\boldsymbol{x}')$ where $\delta(\cdot)$ is the Dirac delta function,

the approximation for f is exact, implying a consistency in the approximation). The interpolant for the gradient of f, $\nabla f(\boldsymbol{x})$, can be obtained in the same manner, so

$$\left\langle \nabla f(\boldsymbol{x}) \right\rangle = -\int_{\Omega} f(\boldsymbol{x}')\nabla W(\boldsymbol{x}-\boldsymbol{x}', h)d\boldsymbol{x}'.$$

A number of kernel functions (e.g., cubic spline, Gaussian kernel, quintic kernel) has been used in the SPH methodology. In this paper, the Wendland C^2 function [20] is used as the kernel in our SPH implementation:

$$W(q,h) = \alpha_d \begin{cases} (1-q/2)^4(2q+1), & \text{for } 0 \le q < 2\ ; \\ 0, & \text{for } q \ge 2, \end{cases}$$

where $q = |\boldsymbol{x}|/h$ is the normalized distance and α_d is the normalization coefficient, assuming a value of $\alpha_d = 7/\left(4\pi h^2\right)$ in two dimensions and $\alpha_d = 21/\left(16\pi h^3\right)$ in three dimensions. Compared to B-splines kernel functions, the Wendland C^2 function is computationally efficient with a demonstrated stability against the common pairing (or clumping) instability problem[20]. For explosive detonation problems involving large deformations, the smoothing length h associated with particle i can be determined dynamically in terms of the local density ρ using the following equation:

$$\frac{dh_i}{dt} = -\frac{1}{d}\frac{h_i}{\rho_i}\frac{d\rho_i}{dt},$$

where d is the dimension of the problem.

In the discrete SPH formulation, the function f and its gradient ∇f (associated with some fluid quantity) at the position of particle i can then be approximated as a weighted sum over the corresponding property of all its neighboring particles, so

$$\left\langle f(\boldsymbol{x}_i) \right\rangle = \sum_{j=1}^{N} f(\boldsymbol{x}_j) W_{ij} \frac{m_j}{\rho_j}$$

and

$$\left\langle \nabla f(\boldsymbol{x}_i) \right\rangle = -\sum_{j=1}^{N} f(\boldsymbol{x}_j) \nabla W_{ij} \frac{m_j}{\rho_j},$$

where m_j and ρ_j are the masses and densities of the N neighboring particles. The governing equation for the simulation of a three-dimensional (3D) explosive detonation in soil is in the Lagrangian formulation [21], and it consists of the continuity equation, the momentum transport equation, and the energy transport equation which assume the following forms, respectively:

$$\begin{cases} \frac{d\rho}{dt} &= -\rho\frac{\partial v^\beta}{\partial x^\beta}, \\ \frac{dv^\alpha}{dt} &= \frac{1}{\rho}\frac{\partial \sigma^{\alpha\beta}}{\partial x^\beta}, \\ \frac{de}{dt} &= \frac{\sigma^{\alpha\beta}}{\rho}\frac{\partial v^\alpha}{\partial x^\beta}, \end{cases}$$

where t is time; x^β is the βth component of the coordinate vector; ρ is the density; v^α is the αth component of the velocity; and, $\sigma^{\alpha\beta}$ is the $\alpha - \beta$ component of the (total) stress tensor. Within the SPH methodology, the discretized form of the continuity, momentum transport, and energy transport equations for particle i assumes the following forms, respectively:

$$\begin{cases} \frac{\mathrm{d}\rho_i}{\mathrm{d}t} = \sum_{j=1}^{N} m_j v_{ij}^\alpha \cdot \frac{\partial W_{ij}}{\partial x_i^\alpha} & (a), \\ \frac{\mathrm{d}v_i^\alpha}{\mathrm{d}t} = \sum_{j=1}^{N} m_j \left(\frac{\sigma_i^{\alpha\beta} + \sigma_j^{\alpha\beta}}{\rho_i \rho_j} + \Pi_{ij}\delta^{\alpha\beta} \right) \frac{\partial W_{ij}}{\partial x_i^\beta} & (b), \\ \frac{\mathrm{d}e_i}{\mathrm{d}t} = \frac{1}{2}\sum_{j=1}^{N} m_j \frac{p_i + p_j}{\rho_i \rho_j} v_{ij}^\beta \cdot \frac{\partial W_{ij}}{\partial x_i^\beta} + \frac{1}{2\rho_i} S_i^{\alpha\beta}\varepsilon_i^{\alpha\beta} & (c), \end{cases} \tag{1}$$

where ρ_i, m_i, v_i, e_i and p_i are the density, mass, velocity, energy and pressure of particle i, respectively; $d(\cdot)/dt$ denotes the rate of the change of a physical variable; Π_{ij} is the Monaghan-type artificial viscosity; $\boldsymbol{\sigma}$ is the stress tensor; $\boldsymbol{S}$ is the deviatoric stress tensor; $\boldsymbol{\varepsilon}$ is the strain rate tensor; and, $v_{ij}^\alpha = v_i^\alpha - v_j^\alpha$ is the relative velocity of particles i and j. This set of equations is supplemented with an equation of state that relates the pressure of particle i to the associated density and energy, viz.

$$p_i = p(\rho_i, e_i).$$

2.2. Artificial viscosity

The Monaghan-type artificial viscosity has been added to the momentum transport equation both to stabilize the numerical algorithm and to represent the conversion of kinetic energy to heat energy associated with shock phenomena [22]. More specifically, without the addition of this artificial viscosity term in the momentum equation, the SPH formalism is not sufficiently dissipative to avert the interpenetration of two converging gas streams, resulting in a poor representation of shock phenomena in the shock-forming regions. The artificial viscosity results in either an attractive or repulsive force between two particles depending on the separation $\boldsymbol{x_{ij}}$ between two particles i and j (viz., at short ranges, the force between the two particles is repulsive whereas the force describes an attraction at long ranges). The standard SPH form for Monaghan-type artificial viscosity defined for a pair of particles i and j is given by

$$\Pi_{ij} = \begin{cases} \dfrac{-\alpha c_{ij}\phi_{ij} + \beta\phi_{ij}^2}{\rho_{ij}}, & \text{for } \boldsymbol{v_{ij}}\cdot\boldsymbol{x_{ij}} < 0\ ; \\ 0, & \text{for } \boldsymbol{v_{ij}}\cdot\boldsymbol{x_{ij}} \geq 0. \end{cases}$$

Here, $\phi_{ij} = \left(h_{ij}\boldsymbol{v_{ij}}\cdot\boldsymbol{x_{ij}}\right)\Big/\left(|\boldsymbol{x_{ij}}|^2 + (\varphi)^2\right)$, $c_{ij} = \frac{1}{2}(c_i + c_j)$, $\rho_{ij} = \frac{1}{2}(\rho_i + \rho_j)$, and $h_{ij} = \frac{1}{2}(h_i + h_j)$. Furthermore, the relative velocity and separation between particles i and j are given by $\boldsymbol{v_{ij}} = \boldsymbol{v_i} - \boldsymbol{v_j}$ and $\boldsymbol{x_{ij}} = \boldsymbol{x_i} - \boldsymbol{x_j}$. Liu et al [7] found that for simulations of explosive detonation in soil and its concomitant damage to metal structures, good results can be obtained with the following choice of parameters for the Monaghan-type artificial viscosity: namely, $\alpha = 1.0$ and $\beta = 10.0$. Finally, setting $\varphi = 0.1h_{ij}$ prevents the overlapping of two particles as $\boldsymbol{x_{ij}} \to 0$ and circumvents the numerical divergence that can occur in the simulation when two particles approach each other too closely.

2.3. The treatment of multi-material interface with high density ratio

A major challenge in the application of the SPH methodology for the simulation of a 3D explosive detonation in soil and its concomitant effects on a metal structure is the treatment of the discontinuous jump in the material properties at an interface. When the ratio of densities of the materials across the interface is sufficiently large (e.g., transition from a granular medium to a material component in the gaseous phase across the interface), this can result in numerical instabilities in the simulation and a premature termination of the calculations Two different formulations have been used in the SPH methodology for the determination of the rate of change of the density. These two formulations for the time rate of change of the density are given by

$$\frac{\mathrm{d}\rho_i}{\mathrm{d}t} = \sum_{j=1}^{N} m_j(v_i^\alpha - v_j^\alpha)\frac{\partial W_{ij}}{\partial x_i^\alpha}, \tag{2}$$

and

$$\frac{\mathrm{d}\rho_i}{\mathrm{d}t} = \rho_i\sum_{j=1}^{N} \frac{m_j}{\rho_j}(v_i^\alpha - v_j^\alpha)\frac{\partial W_{ij}}{\partial x_i^\alpha}. \tag{3}$$

Both of these formulations are applicable when the density ratio of materials across an interface is less than about two. However, when density ratio is larger than about two, Monaghan [4] recommended the use of Eq. (3) for the determination of the rate of change of the density. In order to address the problem of a large density ratio across an interface, the continuity equation is reformulated using a combination of Eqs (2) and (3) as follows [23]:

$$\frac{\mathrm{d}\rho_i}{\mathrm{d}t} = \sum_{j=1}^{N} \frac{\rho_i + \psi_i\rho_j}{(1+\psi_i)\rho_j} m_j v_{ij}^\alpha \cdot \frac{\partial W_{ij}}{\partial x_i^\alpha}, \tag{4}$$

where

$$\psi_i = \frac{1}{\ln\left(k_i\right)}$$

and

$$k_i = \frac{\rho_{i,\max}}{\rho_{i,\min}}.$$

Here, $\rho_{i,\max}$ and $\rho_{i,\min}$ are the maximum and minimum density of particles in the support domain of particle i, respectively. A perusal of Eq. (4) shows that for a large density ratio ($k_i \to \infty$), $\psi_i \to 0$ so that Eq. (4) reduces to Eq. (3); and, similarly, if the density ratio approaches unity ($k_i \to 1$), then it follows that $\psi_i \to \infty$ implying that Eq. (4) simplifies to Eq. (2). In consequence, Eq. (4) provides a generalized formulation for the determination of the rate of change of the density across an interface for an arbitrary density ratio.

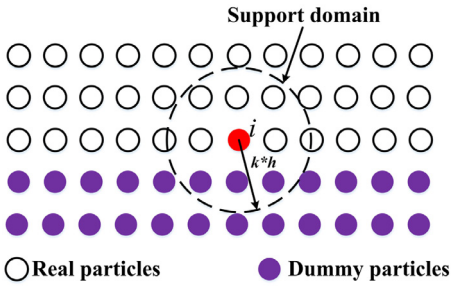

Fig. 1. Types of particles (real and dummy) falling in the support domain of a particle i close to the boundary.

2.4. Boundary treatment

The boundary treatment is a particularly important issue in the SPH methodology. Since Monaghan [24] first proposed the application of the SPH methodology for free surface flows, a number of different formulations for the treatment of a rigid boundary have been proposed [25,26]. This range of formulations to treat boundary data can be classified broadly into three general approaches: (a) virtual or ghost particles [26]; (b) Lennard-Jones potential for repulsive forces on the boundary [27]; and, more recently, (c) boundary integrals [28] for the imposition of complex wall boundary conditions. More specifically, in all these approaches, the boundary is defined by ghost (virtual or dummy) particles that exert repulsive forces on the real particles in order to prevent them from penetrating the solid wall. These ghost particles can be of two types: namely, (1) particles are placed exactly at the solid boundary; and, (2) particles are placed in the region outside the solid boundary and close to it.

In our implementation of SPH, a boundary particle method which can handle arbitrary shape is employed. The method, as shown in Fig. 1, was originally proposed by Adami et al [26] for fluid modeling and was later extended to model boundaries in problems involving large deformations of soils [16]. This boundary treatment uses dummy particles to approximate the interface between the interior fluid domain and the solid wall. It is noted that this generalized wall boundary condition is applicable for the treatment of sharp corners and complex geometries. In this approach, the velocity of the dummy particles involves an extrapolation of the velocity of the adjacent fluid near or at the wall in the interior domain which depends on the wall velocity (whose choice can be used to impose also a free-slip or a no-slip boundary condition at the wall). A pressure boundary condition on the solid particles is used to implicitly enforce the impenetrability condition of a solid wall. Finally, the components of the stress tensor of the dummy particles are extrapolated using the neighboring particles as follows:

$$\sigma_d^{ij} = \frac{\sum_{\kappa=1}^{N} \sigma_\kappa^{ij} W(r_{d\kappa}) - (g^i - a_d^i) \sum_{\kappa=1}^{N} \rho_\kappa r_{d\kappa}^i W(r_{d\kappa}) \delta^{ij}}{\sum_{\kappa=1}^{N} W(r_{d\kappa})},$$

where d and κ are indices for the dummy particles and real particles, respectively. Here, $r_{d\kappa}$ is the distance between a real and a dummy particle; $\boldsymbol{g} \equiv (g^i)$ is the gravitational acceleration; $\boldsymbol{a_d} \equiv (a_d^i)$ is the acceleration of a particle; and, δ^{ij} is the Kronecker delta function [note that the identity matrix $\boldsymbol{I} \equiv (\delta^{ij})$].

2.5. Explicit time integration

The continuity, momentum transport, and energy transport equations [cf. Eqs (1 (a)), (b), and (c)] are integrated in time with a predictor-corrector scheme. As the name implies, this scheme consists of two steps; namely, the predictor step and the corrector step. The predictor step starts from the current value and extrapolates the function value using the gradient of the function. The full discretization of the predictor step for a time step $\Delta t/2$ reads

$$\boldsymbol{x}_i^{t+\frac{\Delta t}{2}} = \boldsymbol{x}_i^t + \frac{\Delta t}{2} \boldsymbol{v}_i^t, \tag{5}$$

$$\boldsymbol{v}_i^{t+\frac{\Delta t}{2}} = \boldsymbol{v}_i^t + \frac{\Delta t}{2} \boldsymbol{a}_i^t, \tag{6}$$

and

$$\rho_i^{t+\frac{\Delta t}{2}} = \rho_i^t + \frac{\Delta t}{2} \left(\frac{d\rho_i}{dt} \right)^t. \tag{7}$$

The components of the stress tensor can be updated in a similar manner to give

$$\boldsymbol{\sigma}_i^{t+\frac{\Delta t}{2}} = \boldsymbol{\sigma}_i^t + \frac{\Delta t}{2}\left(\frac{d\boldsymbol{\sigma}_i}{dt}\right)^t. \tag{8}$$

The corrector step refines the initial approximation obtained by the predictor step to obtain the updated quantity over a time step of size Δt as follows:

$$\boldsymbol{x}_i^{t+\Delta t} = \boldsymbol{x}_i^t + \Delta t \boldsymbol{v}_i^{t+\frac{\Delta t}{2}}, \tag{9}$$

$$\boldsymbol{v}_i^{t+\Delta t} = \boldsymbol{v}_i^t + \Delta t \boldsymbol{a}_i^{t+\frac{\Delta t}{2}}, \tag{10}$$

and

$$\rho_i^{t+\Delta t} = \rho_i^t + \Delta t\left(\frac{d\rho_i}{dt}\right)^{t+\frac{\Delta t}{2}}. \tag{11}$$

In order to simplify the SPH calculations and reduce the amount of data storage, the components of the stress tensor are updated by using the initial approximation value $\boldsymbol{\sigma}_i^{t+\frac{\Delta t}{2}}$ directly to give

$$\boldsymbol{\sigma}_i^{t+\Delta t} = \boldsymbol{\sigma}_i^{t+\frac{\Delta t}{2}} + \frac{\Delta t}{2}\left(\frac{d\boldsymbol{\sigma}_i}{dt}\right)^{t+\frac{\Delta t}{2}}. \tag{12}$$

In order to ensure the stability of the numerical scheme, the time step size for the integration is constrained in accordance to

$$\Delta t = 0.2 \min\left(\left(\frac{h}{\max||\boldsymbol{a}_i||}\right)^{1/2},\ h/c\right),$$

where $\boldsymbol{a}_i$ is the acceleration associated with particle i; c is the speed of sound for each particle, determined from $c = (E/\rho)^{1/2}$ (E is the Young's modulus for the material).

3. Equations of state and constitutive models

3.1. Jones-Wilkins-Lee equation of state

The Jones-Wilkins-Lee (JWL) equation of state (EOS) is used to calculate the pressure of the gaseous products of the explosive detonation [29],

$$p = A\left(1 - \frac{w\eta}{R_1}\right)\exp\left(-\frac{R_1}{\eta}\right) + B\left(1 - \frac{w\eta}{R_2}\right)\exp\left(-\frac{R_2}{\eta}\right) + w\eta\rho_0 E, \tag{13}$$

where $\eta = \rho/\rho_0$ is the density ratio, ρ_0 is the initial density of the explosive, E is the internal energy per unit mass (or, specific internal energy), and w, A, B, R_1, and R_2 are the material parameters of the model, which are obtained by fitting the JWL-EOS model to experimental results.

3.2. Grüneisen equation of state

The Grüneisen EOS is incorporated into the SPH methodology to determine the pressure of a shock-compressed solid [30]. This EOS relates the pressure and density of a solid in following manner:

$$p = \begin{cases} \dfrac{\rho_0 C_0^2 \mu\left[1 + \left(1 - \frac{\gamma}{2}\right)\mu - \frac{\alpha\mu^2}{2}\right]}{\left[1 - (S_1 - 1)\mu - \frac{S_2\mu^2}{\mu+1} - \frac{S_3\mu^3}{(\mu+1)^2}\right]^2} + (\gamma + \alpha\mu)E, & \text{for } \mu > 0\ ; \\ \rho_0 C_0^2 \mu + (\gamma + \alpha\mu)E, & \text{for } \mu \le 0, \end{cases} \tag{14}$$

where $\mu = \left(\rho/\rho_0 - 1\right)$, ρ_0 is the initial density, E is the specific internal energy, and γ, α, S_1, S_2, S_3 and C_0 are the coefficients that characterize the material of interest.

3.3. Elastic-perfectly plastic solid constitutive model

The elastic-perfectly plastic constitutive model is employed to simulate high velocity impact problems [31]. The Jaumann rate of the Cauchy stress ensures that the dynamic response of a material is independent with respect to rotation. With the Jaumann rate, constitutive models based on infinitesimal strain assumption can be used to model problems involving large deformation. The rate of deviatoric part of the Cauchy stress $\dot{S}^{\alpha\beta}$ can be written as

$$\dot{S}^{\alpha\beta} = \dot{S}^{\alpha\beta}_J + S^{\alpha\gamma}\dot{w}^{\beta\gamma} + S^{\gamma\beta}\dot{w}^{\alpha\gamma}. \tag{15}$$

Here, $\dot{w}^{\alpha\gamma}$ is the rotation-rate tensor and $\dot{S}^{\alpha\beta}_J$ is the Jaumann stress rate.

In the elastic range, Hooke's law can be applied, so

$$\dot{S}^{\alpha\beta}_J = 2G\left(\dot{\varepsilon}^{\alpha\beta} - \frac{1}{3}\delta^{\alpha\beta}\dot{\varepsilon}^{\gamma\gamma}\right), \tag{16}$$

where G is the shear modulus and $\dot{\varepsilon}^{\alpha\beta}$ is the strain-rate tensor.

The components of trial elastic deviatoric stress $S^{\alpha\beta}_e$ can be obtained by substituting Eq. (16) into Eq. (15) to give (using the relationship between the trial stress rate and the elastic trial stress)

$$S^{\alpha\beta}_e = \Delta t\left(2G\left(\dot{\varepsilon}^{\alpha\beta} - \frac{1}{3}\delta^{\alpha\beta}\dot{\varepsilon}^{\gamma\gamma}\right) + S^{\alpha\gamma}\dot{w}^{\beta\gamma} + S^{\gamma\beta}\dot{w}^{\alpha\gamma}\right) + S^{\alpha\beta}_{(n)},$$

where $S^{\alpha\beta}_{(n)}$ is the component of the deviatoric stress at n-th time step. The strain-rate tensor and rotation-rate tensor are defined as

$$\dot{\varepsilon}^{\alpha\beta} = \frac{1}{2}\left(\frac{\partial v^{\alpha}}{\partial x^{\beta}} + \frac{\partial v^{\beta}}{\partial x^{\alpha}}\right)$$

and

$$\dot{w}^{\alpha\beta} = \frac{1}{2}\left(\frac{\partial v^{\alpha}}{\partial x^{\beta}} - \frac{\partial v^{\beta}}{\partial x^{\alpha}}\right).$$

The components of the discretized strain-rate and rotation-rate tensors can be obtained using the SPH methodology from

$$\dot{\varepsilon}^{\alpha\beta}_i = \frac{1}{2}\sum_{j=1}^{N}\frac{m_j}{\rho_j}\left(v^{\alpha}_{ji}\frac{\partial W_{ij}}{\partial x^{\beta}_i} + v^{\beta}_{ji}\frac{\partial W_{ij}}{\partial x^{\alpha}_i}\right)$$

and

$$\dot{w}^{\alpha\beta}_i = \frac{1}{2}\sum_{j=1}^{N}\frac{m_j}{\rho_j}\left(v^{\alpha}_{ji}\frac{\partial W_{ij}}{\partial x^{\beta}_i} - v^{\beta}_{ji}\frac{\partial W_{ij}}{\partial x^{\alpha}_i}\right),$$

where $v^{\alpha}_{ji} = v^{\alpha}_j - v^{\alpha}_i$. The second invariant J_2 of the deviatoric part of the elastic trial stress $S^{\alpha\beta}_e$ is

$$J_2 = \frac{1}{2}S^{\alpha\beta}_e S^{\alpha\beta}_e.$$

The material (metal in our case) is still in the elastic range if the second invariant of J_2 is less than one-third of the square of the yield stress σ_Y. Otherwise, the deviatoric stress tensor is calculated using the classical radial return algorithm,

$$S^{\alpha\beta} = \begin{cases} S^{\alpha\beta}_e, & \text{if } J_2 \le \sigma_Y^2/3\ ; \\ \sqrt{\frac{\sigma_Y^2}{3J_2}}S^{\alpha\beta}_e, & \text{if } J_2 > \sigma_Y^2/3. \end{cases} \tag{17}$$

The Johnson-Cook visco-plastic constitutive model which accounts properly for large strains, high strain rates, and high temperature is employed to treat plasticity, so

$$\sigma_Y = \left[A + B(\varepsilon_p)^n\right]\left[1 + C\ln\left(\frac{\dot{\varepsilon_p}}{\dot{\varepsilon_0}}\right)\right]\left[1 - (T^*)^k\right],$$

where A, B, C, n, k are the constant coefficient of metal materials; ε_p is plastic strain; $\dot{\varepsilon_p}$ is plastic strain rate; $\varepsilon_0 = 1s^{-1}$ is reference strain rate; the dimensionless temperature T^* is determined from

$$T^* = \frac{T - T_{\text{room}}}{T_{\text{melt}} - T_{\text{room}}}.$$

Here, T, T_{room}, and T_{melt} are the temperature, room temperature, and melt temperature, respectively. The incremental plastic work of the material (metal) is determined from

$$\Delta W_p^{(n)} = \frac{1}{2}\left(\sigma_p^{(n+1)} + \sigma_p^{(n)}\right)\Delta\varepsilon_p^{(n)}\left(\frac{m}{\rho^{(n+1/2)}}\right),$$

where σ_p at the $(n+1)$-th time step is calculated from the deviatoric stress tensor $\mathbf{S}_e^{(n+1)}$ as follows:

$$\sigma_p^{(n+1)} = \left(\frac{3}{2}\mathbf{S}_e^{(n+1)} : \mathbf{S}_e^{(n+1)}\right)^{1/2}.$$

The incremental plastic strain is given by

$$\Delta\varepsilon_p^{(n)} = \frac{\sigma_p^{(n)} - \sigma_Y}{3G}.$$

3.4. Elastoplastic soil constitutive model

The elastoplastic constitutive model is applied to predict the dynamic behavior of the soil [19,32]. The Drucker-Prager yield criterion is used to determine whether a material has undergone plastic yielding, in accordance to the following relationship:

$$f(I_1, J_2) = \sqrt{J_2} + \varphi_\phi I_1 - k_c \geq 0,$$

where I_1 is the first invariant of the Cauchy stress and J_2 is the second invariant of the deviatoric part of the Cauchy stress. The constants φ_ϕ and k_c are expressed in terms of the internal friction angle ϕ and the cohesion c in accordance to

$$\varphi_\phi = \frac{\tan\phi}{\sqrt{9 + 12\tan^2\phi}}$$

and

$$k_c = \frac{3c}{\sqrt{9 + 12\tan^2\phi}}.$$

The Jaumann rate is used in order to guarantee the objectivity (frame independence) of the stress rate, so

$$\mathring{\boldsymbol{\sigma}} = \dot{\boldsymbol{\sigma}} + \boldsymbol{\sigma}\dot{\boldsymbol{\omega}} - \dot{\boldsymbol{\omega}}\boldsymbol{\sigma}.$$

With the Jaumann rate of stress, the rate of change of the components of the stress tensor in the plastic range can be obtained from

$$\frac{\mathrm{d}\sigma_i^{\alpha\beta}}{\mathrm{d}t} = \sigma_i^{\alpha\gamma}\dot{w}_i^{\beta\gamma} + \sigma_i^{\gamma\beta}\dot{w}_i^{\alpha\gamma} + 2G\left(\dot{\varepsilon}_i^{\alpha\beta} - \frac{1}{3}\delta_i^{\alpha\beta}\dot{\varepsilon}_i^{\gamma\gamma}\right) + K\dot{\varepsilon}_i^{\gamma\gamma}\delta_i^{\alpha\beta} - \dot{\lambda}_i\left[9K\sin\psi\,\delta^{\alpha\beta} + \frac{G}{\sqrt{J_2}}S_i^{\alpha\beta}\right]. \tag{18}$$

The elastic bulk modulus K and shear modulus G are determined, respectively, as follows:

$$K = \frac{E}{3(1-2\nu)} \tag{19}$$

and

$$G = \frac{E}{2(1+\nu)}. \tag{20}$$

The plastic multiplier $\dot{\lambda}_i$ is determined in accordance to the following relationship:

$$\dot{\lambda}_i = \frac{3\varphi_\phi K\dot{\varepsilon}_i^{\gamma\gamma} + (G/\sqrt{J_2})S_i^{\alpha\beta}\dot{\varepsilon}_i^{\alpha\beta}}{27\varphi_\phi K\sin\psi + G}.$$

In the elastoplastic constitutive model, the state of stress of the soil should not lie outside of the yield surface. However, the stress state of the soil may leave the elastic domain during the course of the simulation owing to presence of numerical errors in the computation. To address this problem, the following return mapping algorithm is used to provide an estimate of the stress state of the yield surface when this state exceeds the apex (maximum) of this surface:

$$\overline{\sigma}^{\alpha\beta} = \begin{cases} \sigma^{\alpha\beta} - \frac{1}{3}\left(I_1 - \frac{k_c}{\varphi_\phi}\right)\delta^{\alpha\beta}, & \text{if } -\varphi_\phi I_1 + k_c < 0\ ; \\ \sigma^{\alpha\beta}, & \text{if } -\varphi_\phi I_1 + k_c \geq 0. \end{cases}$$

Similarly, when the stress state of the soil exceeds the yield surface of the Drucker-Prager yield criterion, the components of the deviatoric stress are determined from

$$\overline{\overline{\sigma}}^{\alpha\beta} = \begin{cases} R\overline{\sigma}^{\alpha\beta} + \frac{1}{3}I_1\delta^{\alpha\beta}, & \text{if } -\varphi_\phi I_1 + k_c < \sqrt{J_2}\ ; \\ \overline{\sigma}^{\alpha\beta}, & \text{if } -\varphi_\phi I_1 + k_c \geq \sqrt{J_2}. \end{cases}$$

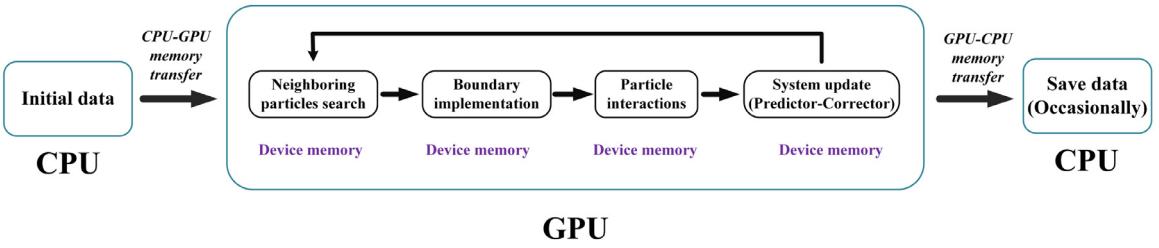

Fig. 2. A flow chart summarizing the major components of the GPU-accelerated SPH methodology.

3.5. Elasto-viscoplastic soil constitutive model

The elasto-viscoplastic constitutive model proposed by Dunatunga and Kamrin [33] is an alternative model that can be used to predict the dynamic behavior of the soil. This constitutive model allows the material to change through many common phases. If the soil is dense, it is treated as an elasto-viscoplastic material that obeys a yield criterion. When the density of the material decreases to a critical level, the material is regarded as a disconnected media. With reference to the Jaumann rate of stress, the evolution of the trial elastic stress in the elasto-viscoplastic constitutive model can be determined from

$$\sigma_{\mathrm{tr}}^{\alpha\beta} = \Delta t\left(\sigma^{\alpha\gamma}\dot{\omega}^{\beta\gamma} + \sigma^{\gamma\beta}\dot{\omega}^{\alpha\gamma} + 2G\left(\dot{\varepsilon}^{\alpha\beta} - \frac{1}{3}\delta^{\alpha\beta}\dot{\varepsilon}^{\gamma\gamma}\right) + K\dot{\varepsilon}^{\gamma\gamma}\delta^{\alpha\beta}\right) + \sigma^{\alpha\beta},$$

where the coefficients K and G are calculated in accordance to Eqs (19) and (20), respectively. The numerical algorithm for the elasto-viscoplastic model proceeds in accordance to the following steps:

1. When the density of a given particle ρ^{n+1} is less than a critical value ρ_c, the stress tensor of the particle is determined as $\boldsymbol{\sigma}^{n+1} = 0$ for the $(n+1)$th step.
2. For all other cases, this model proceeds with the trial elastic stress commonly used in computational plasticity. When the trial pressure is less than 0, we set $\boldsymbol{\sigma}^{n+1} = 0$ and $p_{\mathrm{tr}} = -\frac{1}{3}\mathrm{tr}\left(\boldsymbol{\sigma}_{\mathrm{tr}}\right)$.
3. For the rest of the cases, the stress tensor is determined in the following manner. If $\overline{\tau}_{\mathrm{tr}} \le S_0$ where $\overline{\tau}_{\mathrm{tr}} = \left(\frac{1}{2}\left(\boldsymbol{S}_{\mathrm{tr}} : \boldsymbol{S}_{\mathrm{tr}}\right)\right)^{1/2}$ and $S_0 = \mu_s p_{\mathrm{tr}}$, the granular material is in the elastic range, and the stress tensor $\boldsymbol{\sigma}^{n+1} = \boldsymbol{\sigma}_{\mathrm{tr}}$. If $\overline{\tau}_{\mathrm{tr}} > S_0$, the granular material is in the regime of plasticity, and $\overline{\tau}^{n+1}$ is determined from

$$\left(\overline{\tau}^{n+1}\right)^2 - B\overline{\tau}^{n+1} + H = 0.$$

$\overline{\tau}^{n+1}$ can be obtained explicitly from the quadratic equation immediately above,

$$\overline{\tau}^{n+1} = \frac{2H}{B + \left(B^2 - 4H\right)^{1/2}},$$

where B and H are obtained from $B = S_2 + \overline{\tau}_{\mathrm{tr}} + \alpha$ and $H = S_2\overline{\tau}_{\mathrm{tr}} + S_0\alpha$. In addition, S_2 and α are calculated from $S_2 = \mu_2 p_{\mathrm{tr}}$ and $\alpha = \xi G\Delta t\, p_{\mathrm{tr}}$, where μ_s is a friction coefficient at a static state, μ_2 is the maximum value of the friction coefficient, and ξ is a coefficient of granular material. The stress tensor of each particle can be updated at the end of the step as

$$\boldsymbol{\sigma}^{n+1} = \frac{\overline{\tau}^{n+1}}{\overline{\tau}_{\mathrm{tr}}}\boldsymbol{S}_{\mathrm{tr}} - p_{\mathrm{tr}}\boldsymbol{I}. \tag{21}$$

4. GPU Implementation of SPH methodology

The computational effort required in the SPH methodology is prohibitive owing to the large number of particles required to perform a 3D simulation for real-world applications (e.g., wave breaking phenomena, impact fracture in solid mechanics, study of astrophysical phenomena). Typically, an acceleration technique is required to conduct SPH simulations and, in this paper, we will use GPU technology for this purpose. Our GPU SPH scheme is depicted in Fig. 2 and utilizes the CUDA language and the software development kit (SDK) released by NVIDIA for their family of GPUs (e.g., Tesla, GeForce, Quadro).

The open-source GPU-SPH solver SPHysics is developed to study free-surface flow phenomena and fluid-structure interaction problems, and they can not solve 3D explosion problems directly [17]. Compared to the open-source solver, the energy has been considered and the updating of the smoothing length has been employed in our SPH solver, so that the explosion problems can be simulated. The components in our GPU-accelerated implementation of the SPH methodology for the simulation of explosive detonation in soil are illustrated in Fig. 2. The computationally intensive parts of the SPH simulation were off-loaded to the GPU, while the host central processing unit (CPU) was delegated to provide the initial data

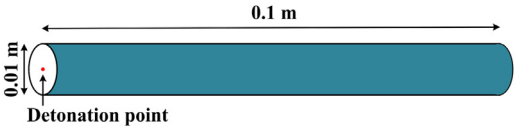

Fig. 3. The initial configuration of 3D C4 slab detonation.

for the problem and to (occasionally) save the results of the simulation to the hard disk. The data for the SPH simulation resides in the device memory of GPU in order to minimize the latency involved in CPU-GPU data transfers. The following computationally intensive tasks were performed with kernels executed by GPU: (1) the construction of the list of neighbors for each particle used in the simulation; (2) the computation of the interaction of each particle with its neighbors and with the boundaries in the computational domain; and, (3) update of the fluid properties of each particle by integrating over a given time step Δt.

The initial data is prepared in the CPU and transferred to the GPU. A linked-list algorithm is used to construct a neighbor list for each of the particles used in the simulation [34,35]. This involves partitioning the computational domain with a regular grid with cubic cells of the size of the support domain of the kernel, indexing the particles by the cell they reside in and sorting them in accordance to their index. The neighbor list for each particle can be constructed by considering only those particles in the nearest neighbor cells of the particle. Next, the CUDA kernel for the force computation is undertaken involving the determination of the interaction between particle i and its neighbors [viz., the sum of the right-hand sides of Eq (1)]. Once these particle-particle interactions are computed, the state of the fluid system can be updated by numerical integration (here, as mentioned previously, a predictor-corrector algorithm is used). For particles interaction and time integration, we launch a grid of compute threads in the GPU, with each thread responsible for the computations associated with a single particle. At the end of this process, the updated physical variables are transferred from the GPU to the CPU and saved to the hard disk (at user-specified intervals).

The solution procedure for the numerical simulation of the interaction between aluminium structure and explosion in soil is shown in Algorithm 1. All the simulations reported herein were conducted on a PC with a single NVIDIA GeForce

Algorithm 1 The algorithm for simulation of interaction between aluminium structure and explosion in soil.

1. Input: ρ_i, $\boldsymbol{x}_i$, $\boldsymbol{v}_i$, and e_i at $t = t_n$;
2. Neighboring particles search using modified linked-list search algorithm (see details in [35]);
3. Implementation of boundary condition (see Section 2.4);
4. Calculate p_i (see Eq. (13) and Eq. (14)) and $S_i^{\alpha\beta}$ (see Eq. (17), Eq. (18), and Eq. (21)) at $t = t_n$;
5. Compute $\frac{\mathrm{d}\rho_i}{\mathrm{d}t}$, $\frac{\mathrm{d}v_i^\alpha}{\mathrm{d}t}$, and $\frac{\mathrm{d}e_i}{\mathrm{d}t}$ at $t = t_n$ (see Eq. (1);
6. Compute ρ_i, $\boldsymbol{x}_i$, $\boldsymbol{v}_i$, and e_i at $t = t_{n+\frac{1}{2}}$ (see Eq. (5) to Eq. (8) in Section 2.5);
7. Neighboring particles search using modified linked-list search algorithm;
8. Implementation of boundary condition (see Section 2.4);
9. Calculate p_i (see Eq. (13) and Eq. (14)) and $S_i^{\alpha\beta}$ (see Eq. (17), Eq. (18), and Eq. (21))at $t = t_{n+\frac{1}{2}}$;
10. Compute $\frac{\mathrm{d}\rho_i}{\mathrm{d}t}$, $\frac{\mathrm{d}v_i^\alpha}{\mathrm{d}t}$, and $\frac{\mathrm{d}e_i}{\mathrm{d}t}$ at $t = t_{n+\frac{1}{2}}$ (see Eq. (1));
11. Output: ρ_i, $\boldsymbol{x}_i$, $\boldsymbol{v}_i$, and e_i at $t = t_{n+1}$ (see Eq. (9) to Eq. (12) in Section 2.5);

RTX 2080 Ti graphics card. The parallel efficiency of the GPU-accelerated SPH solver will be demonstrated in our numerical simulations of 3D explosive detonation in soil.

5. Validation of the methodology

In this section, the various components of the proposed the GPU-accelerated SPH method (e.g., the JWL and Grüneisen EOSs, the elastic-perfectly plastic constitutive model, the elastoplastic soil constitutive model, and the phase-change constitutive model) will be validated using four benchmark test cases.

5.1. Case 1: 3D C4 explosive detonation

The JWL EOS implemented in our GPU-accelerated SPH solver is validated using a test case involving the 3D explosive detonation of a C4 slab. The initial configuration of the 3D C4 slab is displayed in Fig. 3. This test case consists of a 0.1 m long C4 slab with a diameter of 0.01 m that is detonated at one end. In this example, the boundaries of the C4 slab are treated as a free surface in the SPH simulation. The initial particle spacing (before the detonation) was uniform along the slab, with a separation between particles of $\Delta x = 0.15385$ mm. A total of 2,145,000 particles were used for this simulation with an initial smoothing length of $h = 1.5 \times \Delta x = 0.230775$ mm. In order to confirm the computational stability of this simulation, the time step for this case was set as $\Delta t = 1.0 \times 10^{-9}$ s. The coefficients for the JWL EOS for C4 are summarized

Table 1
Coefficients used in the JWL EOS for C4 and TNT[36].

Explosive	ρ_0 (kg m^{-3})	A (Pa)	B (Pa)	R_1	R_2	w	E_0 (J kg^{-1})
C4	1601	6.098×10^{11}	1.3×10^{10}	4.5	1.4	0.25	5.621×10^{6}
TNT	1630	3.172×10^{11}	3.219×10^{9}	4.15	0.95	0.30	4.29×10^{6}

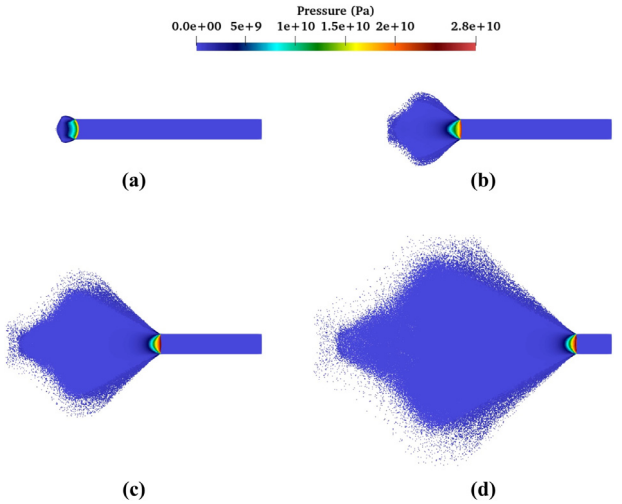

Fig. 4. The temporal evolution of the pressure distribution arising from the explosive detonation of a 3D C4 slab at four different times after the initial detonation: (a) 1 μs; (b) 3 μs; (c) 6 μs; and, (d) 10 μs.

Table 2
Parameters used in the Johnson-Cook constitutive model for Aluminium [38] and Armco iron [11].

Material	A (MPa)	B (MPa)	C	n	k	T_{room} (K)	T_{melt} (K)
Iron	175	380	0.0015	0.34	1.0	273	775
Aluminium	175	380	0.06	0.32	0.55	293	1811

in Table 1. Once the C4 explosive is ignited at one end (cf. Fig. 3), the detonation shock wave propagates along the C4 slab at a constant velocity of 8,193 m s^{-1}. In consequence, the detonation wave reaches the opposite end of the C4 slab in 12.21 μs.

The temporal evolution of the pressure distribution at four different times, namely at 1 μs, 3 μs, 6 μs and 10 μs after the initial detonation is depicted in Fig. 4. After the activation of the explosive slab, a compressive spherical shock wave is generated and propagates along the slab. When the shock wave reaches the free surface of the slab, a rarefaction wave is generated and propagates inward. Subsequently, the gaseous products expand outward with a decrease in density and pressure due to the free surface boundary condition imposed at the outer surface of the C4 slab. It is seen that the pressure reaches the maximum value along the centerline of the C4 explosive slab. Furthermore, it can be noted that the predicted value of the peak pressure for the 3D C4 detonation is consistent with the reported experimental value of 28 GPa [36].

5.2. Case 2: 3D taylor bar impact

In this section, we aim to demonstrate the performance of the method in modeling large deformation of metals. The elastic-perfectly plastic constitutive model and the Grüneisen EOS will be validated using a cylindrical Taylor bar impact test case. Woodward et al [37] developed a simple impact configuration for the evaluation of dynamic flow stress of a projectile using Taylor impact tests. The initial configuration of the Taylor bar impact test is shown in Fig. 5. The material of the cylindrical Taylor bar is Armco iron, and this bar impacts a rigid (solid) boundary vertically at a velocity 220 m s^{-1}. The initial length L_0 and diameter D_0 of the cylindrical Taylor bar are 25.46 mm and 7.6 mm, respectively. For the SPH simulation for this test case, there are 158,427 particles evenly distributed along the cylindrical bar with an initial particle spacing of $\Delta x = 0.22$ mm. Three layers of dummy particles were used to simulate the solid (rigid) walls with SPH. The time step of case was set as $\Delta t = 1.0 \times 10^{-8}$ s. The parameters of the elastic-perfectly plastic constitutive model (or, Johnson-Cook model) and the Mie-Grüneisen EOS used in our simulations of the Taylor bar impact test case are summarized in Tables 2 and 3, respectively.

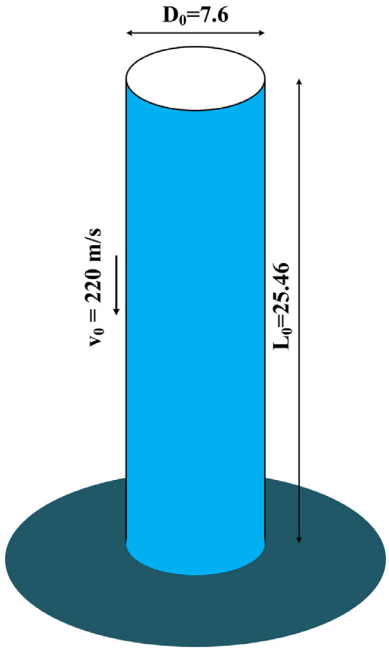

Fig. 5. The initial configuration of the 3D Taylor bar impact test (all dimensions for length are in mm).

Table 3
Parameters used for the Mie-Grüneisen EOS for Aluminium [39] and Armco iron [11].

Material	ρ_0 (kg m^{-3})	C_0 (km s^{-1})	S_1	S_2	S_3	γ	α	E_0 (J)
Iron	7890	3.63	1.80	0	0	1.81	0.46	0
Aluminium	2700	5.24	1.40	0	0	1.97	0.48	0

Table 4
Comparison of predicted and experimental results for the dimensions of a deformed Armco iron cylinder following a Taylor impact test.

	Experiment [40]	Predicted	Error (%)
L (mm)	19.8	19.5	1.5
D (mm)	13.7	14.7	6.8
W (mm)	8.6	8.2	4.6

The predicted pressure distribution at four different times, namely at 10 μs, 40 μs, 60 μs and 80 μs after the initial impact, is shown in Fig. 6. Firstly, a wave of compressive stress is generated at the impact surface (cf. Fig. 6(a)). As the event proceeds, the elastic and plastic compressive waves arrive at the opposite end of the Taylor cylindrical bar, causing the cylinder to deform significantly. Subsequently, these compressive wave are reflected as tensile waves of similar magnitude, and these tensile waves interact with the compressive stress resulting in an overall reduction of the stress state. After repeated propagation and reflection of the compressive and tensile waves in the cylindrical bar, the amplitudes of the compressive and tensile stresses diminish in time and eventually decrease to zero (cf. Fig. 6(d)). A comparison of the prediction of the dimensions of the deformed cylinder after the Taylor impact test obtained from our SPH simulation with some experimental data [40] is shown in Table 4. In this table, L is the deformed length of the cylinder, D is the deformed diameter of the cylinder, and W is the bulge (diameter of the deformed cylinder at a height of $0.2L_0$ from the deformed end where L_0 in the original length of the cylinder). Table 4 quantifies the degree of agreement between the predicted SPH results and the experimental measurements in terms of a relative error:

$$\text{Error } (\%) = 100 \times |\text{Predicted} - \text{Experiment}| \Big/ \text{Experiment}. \tag{22}$$

A perusal of the table shows that the differences between the predicted and experimental results for the deformed cylinder dimensions differ by less than 7% with the smallest discrepancy being the deformed length L and the largest discrepancy being the deformed diameter D. Overall, we note that our SPH methodology provides generally very good predictions for the deformation of an Armco iron cylinder following an intense impulsive loading resulting from a high-velocity impact.

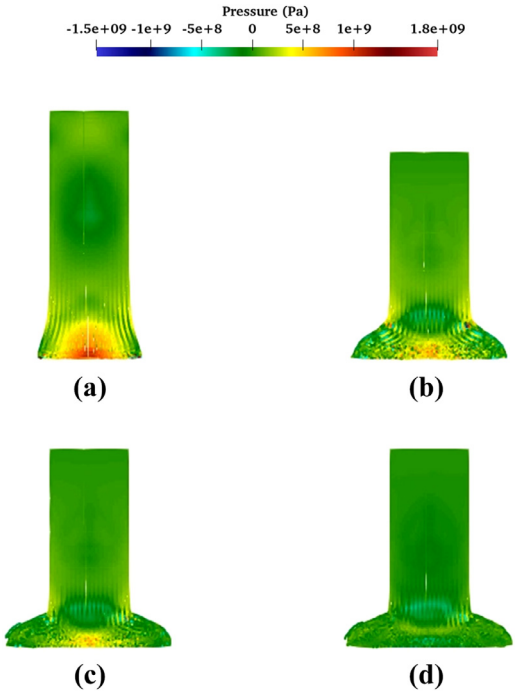

Fig. 6. The temporal evolution of the pressure distribution in a Taylor cylindrical bar is shown at four different times; namely, at (a) 10 μs, (b) 40 μs, (c) 60 μs, and (d) 80 μs after the initial impact.

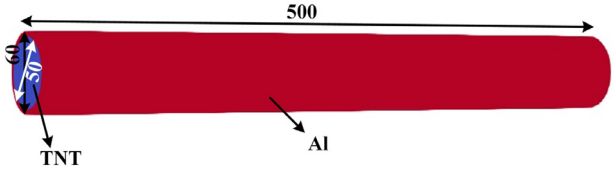

Fig. 7. The initial configuration of 3D expansion of cylinder aluminium caused by TNT detonation (all dimensions for length are in mm).

5.3. Case 3: 3D expansion of al cylinder generated by TNT detonation

In order to further verify the explosive detonation model and elastic-perfectly plastic constitutive model, the expansion of an Al cylindrical shell caused by the trinitrotoluene (TNT) explosive detonation is simulated. The initial geometry of this numerical case is shown in Fig. 7. The initial particle spacing was 1 mm, and a total of 1,305,500 particles were involved in this numerical case. The parameters of the Johnson-Cook constitutive model and the Mie-Grüneisen EOS for Al are summarized in Table 2 and 3. The temporal evolution of the velocity distribution of the expansion of aluminium cylinder at four different times, namely at 10 μ, 20 μ, 30 μ, and 40 μ is shown in Fig. 8. After the TNT explosive detonation, most of the internal energy generated by the exposive detonation is transferred to the kinetic energy of the surrounding Al cylinder, and then the Al cylinder expands outwards rapidly. In addition, as depicted in Fig. 9, the radial deformation of the Al cylinder obtained from SPH has been compared against the experimental data from [41]. It can be observed that the curve of numerical radial deformation of aluminium shell is very similar to the experimental data. Taken together, this suggests that our SPH methodology is capable of providing good predictions for the explosive detonation and the large deformation of Al cylinder caused by explosive detonation.

5.4. Case 4: 3D sand collapse problem

The elastoplastic constitutive and elasto-viscoplastic constitutive models, implemented in our in-house SPH code, will be validated using the test case involving the collapse of a 3D sand pile (involving as such the phenomenology associated with dynamic large deformation of soil). Lube et al [42] presented experimental observations of the axisymmetric collapse of vertical columns of sand. As shown in Fig. 10, the granular material is initially confined in a cylindrical container. Subsequently, the cylindrical container is removed rapidly and the granular media is allowed to spread out on a flat surface. The aspect ratio of the sand column $a_i = h_i/d_i$ determines the characteristics of the collapse of the sand column where h_i is the initial

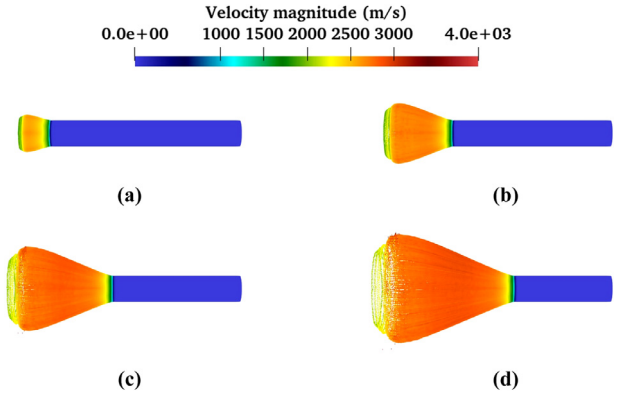

Fig. 8. The temporal evolution of the velocity distribution of the Al cylinder arising from the explosive detonation of a 3D TNT slab at four different times after the initial detonation: (a) 10 μs; (b) 20 μs; (c) 30 μs; and, (d) 40 μs.

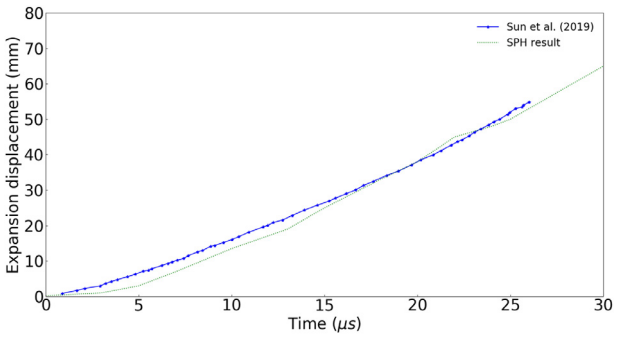

Fig. 9. Comparison of the temporal evolution of the radial displacement of the expansion of an aluminium cylindrical shell obtained from experiment data [41] with numerical results obtained using SPH.

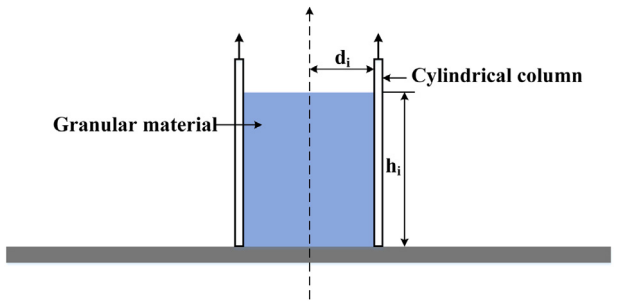

Fig. 10. The initial geometry for the 3D sand collapse problem involving a confined cylindrical sand column with height h_i and radius d_i.

Table 5
The parameters of the elastoplastic and elasto-viscoplastic constitutive models for the sand collapse problem [33].

			Elastoplastic model constants			Elasto-viscoplastic model constants			
ρ_0 (kg m^{-3})	E (MPa)	ν	ϕ (°)	ψ (°)	c (kPa)	ρ_c (kg m^{-3})	ξ (m$^{1/2}$ kg$^{-1/2}$)	μ_s	μ_2
1379	21.6	0.30	37.0	0.0	0.0	500	1.1233	0.6419	0.8435

height and d_i is the initial radius of the cylindrical sand column. In the test case considered here, the initial height h_i and radius d_i of the cylindrical sand column are 100 mm and 200 mm, respectively. For this test case, a total of 482,430 particles were initially distributed evenly along the cylindrical sand column with an initial uniform (constant) particle spacing of 4 mm. The time step for this case was set as $\Delta t = 1.0 \times 10^{-5}$ s. The elastoplastic and elasto-viscoplastic constitutive models coefficients for the sand collapse problem are summarized in Table 5.

The predictions of the velocity distribution using the elastoplastic and elasto-viscoplastic constitutive models at four different times (viz., at 0.05 s, 0.10 s, 0.20 s, and 0.60 s after the initial release of the sand column) are displayed in Fig. 11.

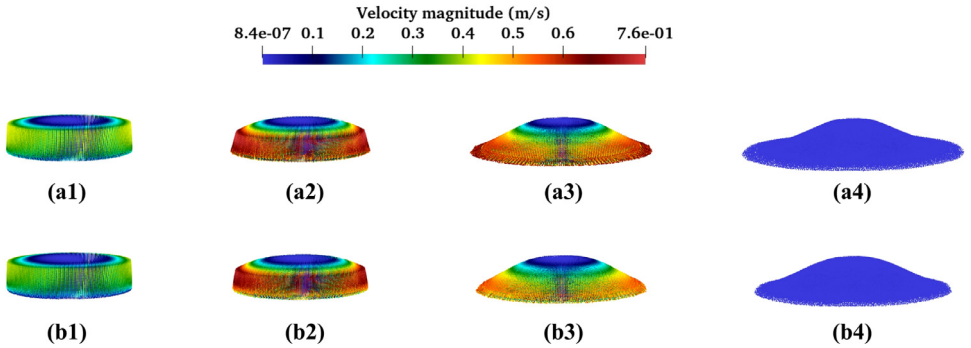

Fig. 11. The temporal evolution of the velocity distribution of the 3D sand collapse problem obtained using the elastoplastic constitutive model (top row labeled using (a)) and the elasto-viscoplastic constitutive model (bottom row labeled using (b)). For each row, the velocity distribution is obtained at four different times after the initial release of the sand column: (a1), (b1) 0.05 s; (a2), (b2) 0.10 s; (a3), (b3) 0.20 s; and, (a4), (b4) 0.60 s.

Table 6
Comparison of the steady-state diameter d_∞ and h_∞ obtained from experimental measurements (Expt) for the 3D sand collapse problem with predictions obtained from SPH simulations using the elastoplastic (Elast) and elasto-viscoplastic (Phase) constitutive models. The steady-state dimensions of the sand pile have been normalized by the initial radius d_i of the sand column. Error_e and Error_p refer to the relative errors between the experimental data and the predictions obtained with the elastoplastic and elasto-viscoplastic constitutive models, respectively.

	Expt (mm)	Elast (mm)	Phase (mm)	Error_e (%)	Error_p (%)
d_∞/d_i	1.62	1.67	1.56	3	3.7
h_∞/d_i	0.5	0.5	0.51	0	2

The upper row in the figure shows the results for the elastoplastic constitutive model, whereas the bottom row exhibits the results for the elasto-viscoplastic constitutive model. The results obtained from the two constitutive models are very similar. Once the granular material is released from the cylindrical container, it is seen to collapse rapidly and a discontinuity in the collapse surface can be observed. Following this, a parabolic profile is formed with the disappearance of the discontinuity (cf. Fig. 11(a3) and (b3) for the elastoplastic and elasto-viscoplastic constitutive models, respectively).

Table 6 summarizes a comparison of the SPH predictions of the steady-state height h_∞ and diameter d_∞ of the sand pile with some experimental measurements obtained by Lube et al [42]. The conformance between the predicted results (obtained with both the elastoplastic and elasto-viscoplastic constitutive models) and the experimental measurements is quantified using the relative error (cf. Eq. (22)). Generally speaking, the relative errors between the predicted and experiments results is less than 4%, with the relative error in the prediction of d_∞ being larger than that for the prediction of h_∞ for both constitutive models. Overall, it is noted that the predictions for the steady-state height and diameter is slightly better for the elastoplastic constitutive model than for the elasto-viscoplastic constitutive model.

6. Simulation of 3D explosive detonation in soil

After the validation of the various components of the GPU-accelerated SPH code reported above, we applied this code to simulate a 3D explosive detonation in soil. To this purpose, both the elastoplastic and elasto-viscoplastic constitutive models were used in the SPH simulations in order to predict the soil fragmentation following the onset of the explosive detonation. In order to directly compare our SPH numerical results with some available experimental data, the initial configuration used in our simulations of an explosive detonation in soil was identical to the experimental setup used by Rigby et al [1].

In consequence, the geometry of the 3D explosive detonation of C4 in soil is depicted Fig. 12. The geometry of this test arrangement consists of a cylindrical container with a diameter of 500 mm and a height of 375mm filled with a granular material. A cylindrical C4 high-energy explosive is buried in this granular media with a depth l_1 of 28 mm (from the free surface of soil down to the upper boundary of the charge). The initial diameter and height of the C4 explosive are 56 mm and 20 mm, respectively.

In this test case, we used a total of 5,500,000 particles in the SPH simulation with an initial particle spacing of 2.5 mm. The time step for this case was $\Delta t = 1.0 \times 10^{-7}$ s. For all the simulations in this section, the material parameters are the same as those given in Tables 1 and and 5, except that the initial density of the soil is set as 1,600 kg m^{-3}, which is same as that in the experiment [1]. The total computational time (wall-clock time) required to simulate the various physical processes in a 0.9 ms interval, following the initial explosive detonation of C4 in the soil, is 5 hours.

The temporal evolution of the velocity distribution for the 3D explosive detonation in the granular media, obtained using the elastoplastic and elasto-viscoplastic constitutive models, are shown in Figs 13 and 14, respectively. It is noted that the

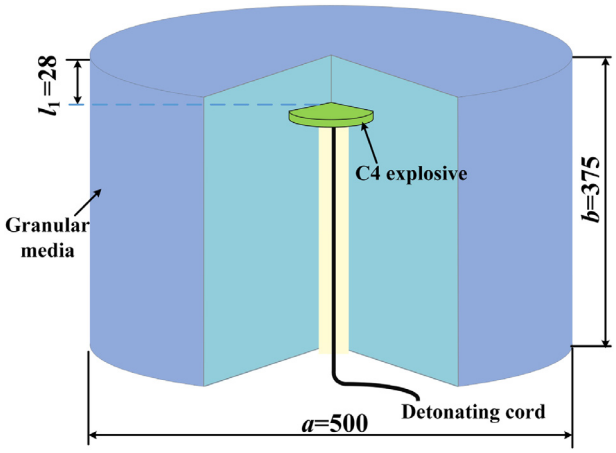

Fig. 12. The initial geometry for the 3D C4 explosive detonation in soil. All dimensions of length are in mm.

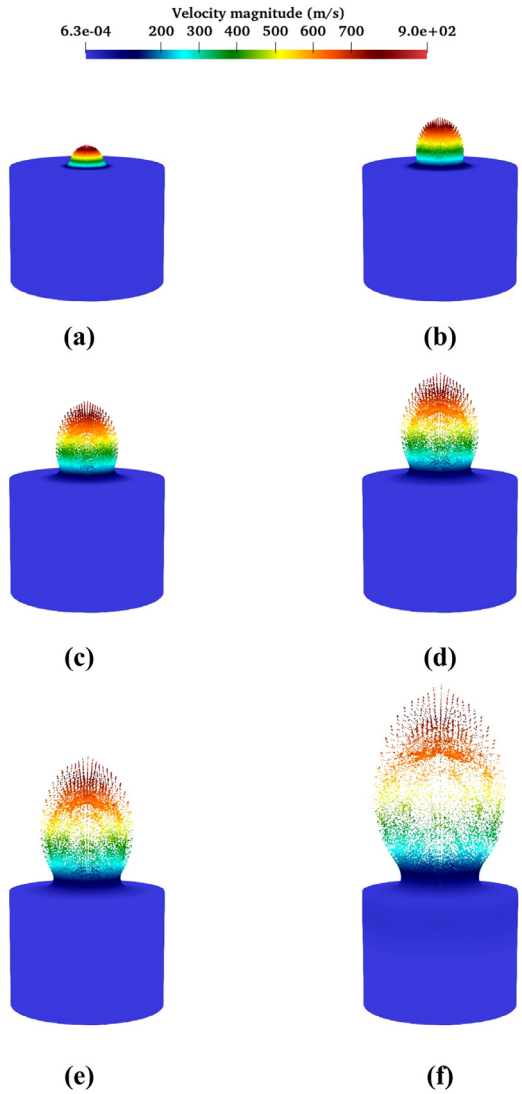

Fig. 13. The temporal evolution of the velocity distribution of the soil resulting from the explosive detonation of C4 obtained using the elastoplastic constitutive model at the following times after detonation: (a) 0.1 ms; (b) 0.2 ms; (c) 0.3 ms; (d) 0.4 ms; (e) 0.5 ms; and, (f) 0.75 ms.

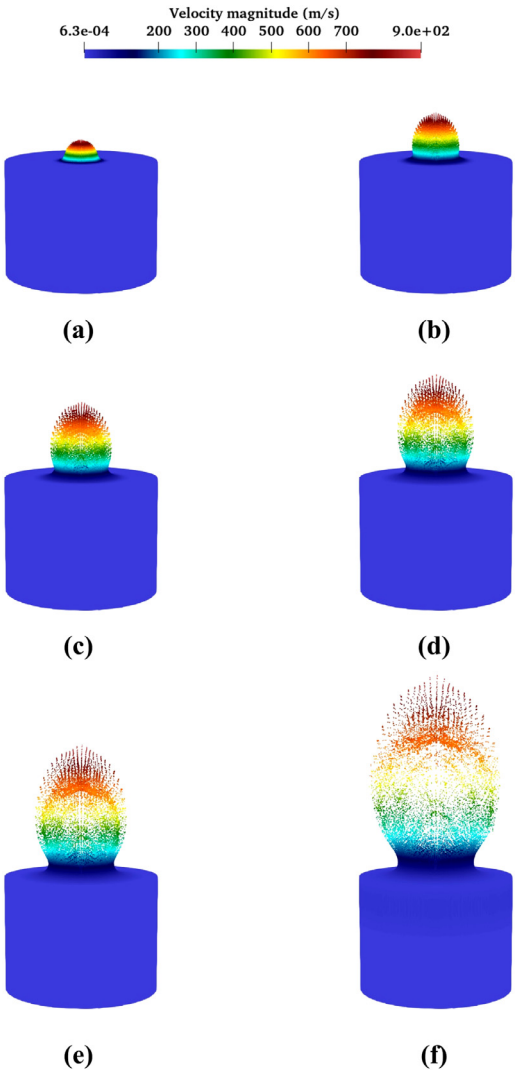

Fig. 14. The temporal evolution of the velocity distribution of the soil resulting from the explosive detonation of C4 obtained using the elasto-viscoplastic constitutive model at the following times after detonation: (a) 0.1 ms; (b) 0.2 ms; (c) 0.3 ms; (d) 0.4 ms; (e) 0.5 ms; and, (f) 0.75 ms.

fragmentation of the soil after the onset of detonation obtained with the elastoplastic constitutive model is very similar to that obtained with the elasto-viscoplastic constitutive model.

After the activation of the C4 high-energy explosive buried in the soil, gaseous products of the detonation with high pressure and velocity are generated. The momenta of these gaseous products are partly transmitted to the soil adjacent to the location of the C4 explosive. As the surrounding soil gains kinetic energy as a result of the detonation and moves swiftly and radially outward, a soil cap with a small volume is formed (see Figs 13(a) and 14(a)). The volume of this soil cap increases monotonically with time owing to the continued work done by the detonation products with high pressure [as is evident by an examination of Figs 13(b), (c), and (d) and Figs 14(b), (c), and (d)]. Finally, a large soil bubble is formed [which can be seen from a perusal of Figs 13(f) and 14(f)].

Figs. 15 and 16 show predictions of temporal development of the pressure distribution in the soil (following the explosive detonation of C4) obtained using the elastoplastic and elasto-viscoplastic constitutive models, respectively. Moreover, a careful examination of these figures reveals the presence of a spherical shock wave propagating in the soil (generated by the C4 explosive detonation). As this shock wave passes through the granular material, the energy of the wave is partly converted to kinetic energy and internal energy of the soil. As a result, the pressure in soil generated by the detonation shock wave is seen to rapidly decrease with increasing propagation distance from the source.

Fig. 17 compares the numerical and experimental results of the soil height as a function of time. The experimental data are taken from the explosive detonations [1,43]. Note that although the test setups in [43] is similar to that in [1], they are not identical. The diameter and thickness of the explosive in [43] are 64 and 20 mm, respectively, giving rise to a

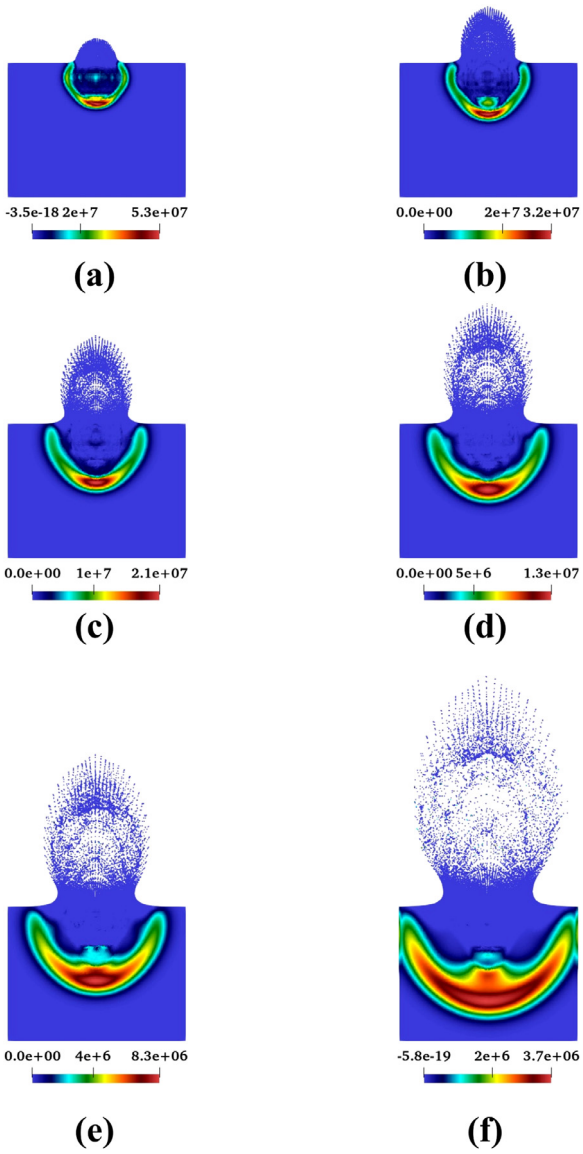

Fig. 15. The temporal evolution of the pressure distribution of the soil resulting from the explosive detonation of C4 obtained using the elastoplastic constitutive model at the following times after detonation: (a) 0.1 ms; (b) 0.2 ms; (c) 0.3 ms; (d) 0.4 ms; (e) 0.5 ms; and, (f) 0.75 ms.

total mass of 100 g. The numerical simulations follow the exact setups in the two experiments. The results in Fig. 17 are obtained with the elastoplastic and elasto-viscoplastic constitutive models. A careful perusal of this figure indicates that the predictions of soil height obtained from the two constitutive models are well corroborated by the experimental data. Particularly, the agreement between the numerical simulation and the data from Grujicic et al [43] is very good, whereas a larger discrepancy is observed when comparing with Rigby et al [1]. Nevertheless, the maximum relative error between the measurements and the predictions is less than about 13.6%. Moreover, it can be seen that the elasto-viscoplastic constitutive model seems to provide slightly better predictions of the soil height as a function of time than those provided by the elastoplastic constitutive model in this case. Even so, the differences in the predictions provided by the two constitutive models are very small and, indeed, we conclude that both of these models captured well the physical processes responsible for soil fragmentation and ejecta following the C4 explosive detonation.

Furthermore, the temporal evolution of pressure at the depth of 11.73 cm (from the top surface of soil to the measured point) in the soil is compared with the experimental data from [43,44] (see Fig. 18). It can be observed that the magnitudes of peak pressue generated by the explosion in soil using these two constitutive models are 55.7 MPa and 54.7 MPa, which are close to the experimental peak pressure.

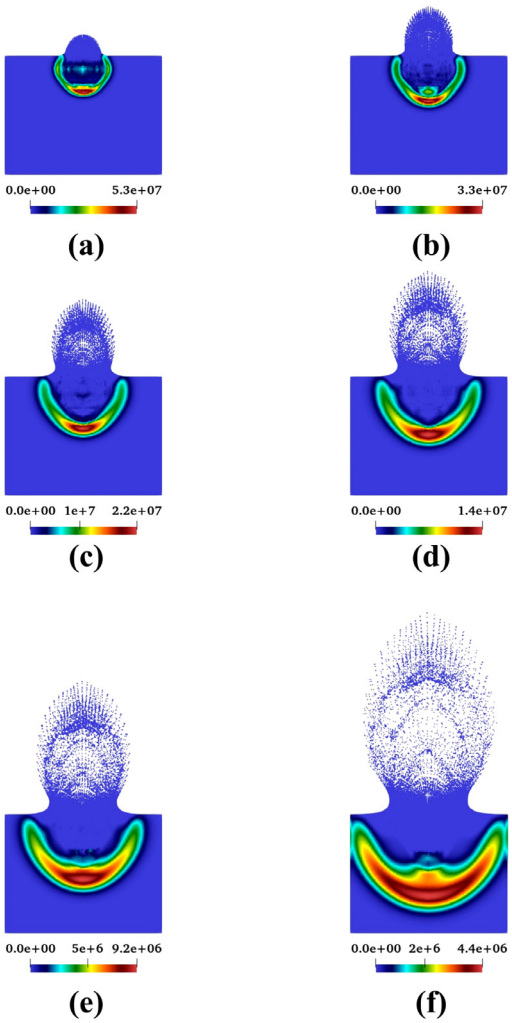

Fig. 16. The temporal evolution of the pressure distribution of the soil resulting from the explosive detonation of C4 obtained using the elasto-viscoplastic constitutive model at the following times after detonation: (a) 0.1 ms; (b) 0.2 ms; (c) 0.3 ms; (d) 0.4 ms; (e) 0.5 ms; and, (f) 0.75 ms.

Table 7
Computational efficiency of the GPU-accelerated SPH code for simulation of the explosion in soil.

Case No.	Particle spacing (mm)	Particle number (million)	FPS (s^{-1})
1	6.25	0.48	24.03
2	4.69	0.90	9.73
3	3.75	1.58	7.18
4	3.12	2.60	4.62

6.1. Computational efficiency

In this section, we investigate the parallel efficiency of our GPU-accelerated SPH code for the case of explosion in soil. The frame per second (FPS), which is defined as the number of computational steps executed in one second of wall clock time, is employed to measure the efficiency. This measurement is independent of the physical time of the problem, the time step size, and the total number of steps; thus, it is more objective than the total used time.

Four simulations of the problem of explosion in soil are carried out with varying resolution. The resulted particle number ranges between 0.48 to 2.60 million. The simulations are performed with a NVIDIA GeForce RTX 2080 Ti card installed on a desktop computer. The average FPS in the four simulations are listed in Table 7. The FPS decreases with increasing particle number; however, even with 2.6 million of particle, the solver still has a FPS of 4.62.

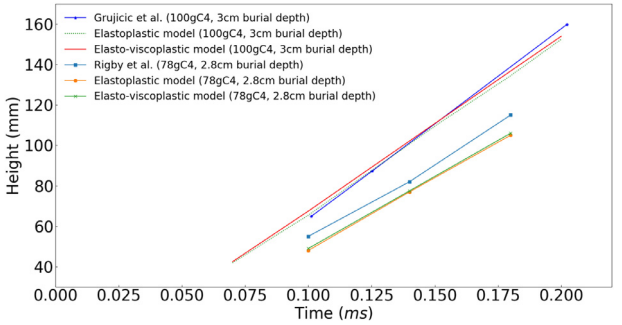

Fig. 17. Comparison of the soil height as a function of time obtained from experimental measurements from [1,43] for the explosive detonation of C4 in soil with predictions obtained from SPH simulations using the elastoplastic and elasto-viscoplastic constitutive models.

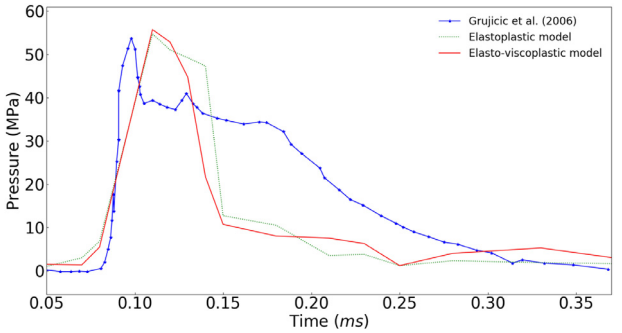

Fig. 18. Comparison of the temporal evolution of the pressure at the depth of 11.73 cm of the soil obtained from experiments [43,44] with numerical data obtained from SPH using the elastoplastic model and elasto-viscoplastic models.

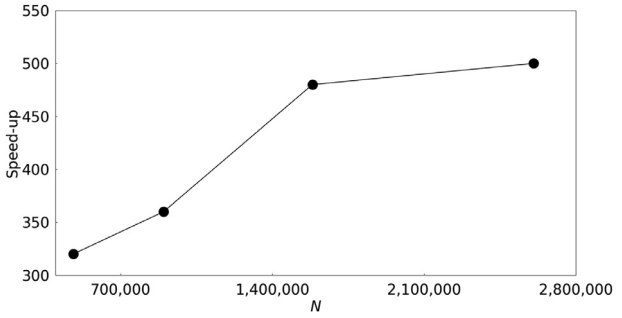

Fig. 19. The speedup of the explosion in soil using a single GPU compared to the simulation using a single CPU.

To further analyse the efficiency of the GPU implementation, we compare the GPU computing with serial CPU computing. For this purpose, a serial CPU solver is developed. The CPU solver follows exactly the same computational process like the GPU solver, except that the CPU solver is without any parallelization. It should be pointed out that the CPU solver does not have a thorough optimization, because some implementations suitable for GPU might not be the best practice in CPU-based serial computing. Nevertheless, the comparison can still provide a rough estimation between the GPU and CPU computing. The speed-up of the GPU solver over the CPU solver is defined as

$$S_p = \frac{\text{FPS with the GPU computing}}{\text{FPS with the serial CPU computing}}. \tag{23}$$

The four simulations listed in Table 7 are simulated again using these two solvers. The CPU simulations are performed with an Intel Xeon silver 4110 processor. Because the simulations based on CPU cannot be finished in a reasonable time, without loss of generality, the FPS is computed based on the information obtained by executing the four simulations for the first 1,000 steps. To make the comparison reasonable, the FPS of GPU computing is also based on the first 1,000 steps. It should be noted that when computing the speed-up, the CPU and GPU simulations have identical particle number and computational conditions.

The speed-up obtained from the four simulations is depicted in Fig. 19. It is seen that the speed-up gradually increases with increasing particle number. The increase of speed-up slows down when the particle number becomes larger. This

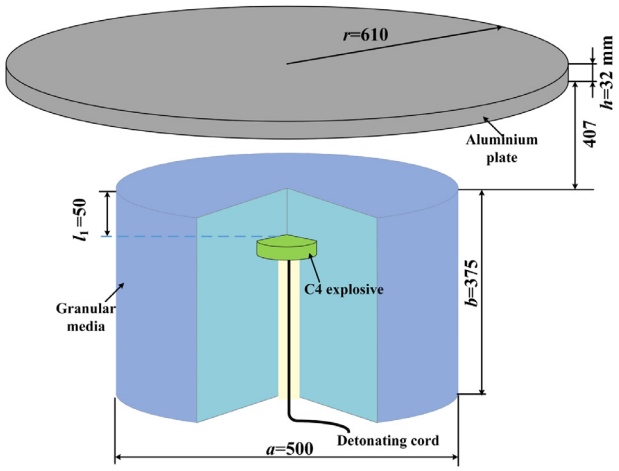

Fig. 20. The initial configuration used for the simulation of the damage incurred by an Al plate resulting from the explosive detonation of a C4 charge embedded in a cylindrical slab of sand. The dimensions for lengths are in mm.

trend is also observed in other studies [14,19]. The reason is that when there are not enough particle in the simulation, the computational power of the GPU device is not fully utilized. From Fig. 19 it can be found that the speed-up is around 500 when 2.6 million of particles are used in the simulation. This high value of speed-up is usually difficult to achieve with parallel CPU computing unless super-computers are employed. On the other hand, it can be conveniently realized with a graphic card installed on a conventional desktop.

7. The damage incurred by an aluminium plate from an explosive detonation in soil

After the simulation of the explosive detonation of C4 in sand, the damage incurred by an Al plate located in the vicinity of the detonation can be modeled. To this purpose, we consider the initial configuration of Al plate and C4 explosive depicted in Fig. 20. The initial geometry for the cylindrical slab of sand and for the location of the C4 explosive embedded in this slab is exactly the same as that described in [45]. For the current test, the bottom side of a cylindrical Al plate with a thickness of 32 mm and a radius of 1,220 mm is positioned at a distance of 407 mm above the top of the cylindrical sand slab. The diameter and thickness of the explosive are 25.4 cm and 7.62 cm, respectively.

For this simulation, a total of 2,000,000 particles were used with an initial spacing between each particle of 3.75 mm. The time step for this numerical case was $\Delta t = 1.0 \times 10^{-7}$ s. The coefficients that define the JWL EOS (for the C4 explosive), the Grüneisen EOS (for iron) and the elastoplastic and elasto-viscoplastic constitutive models (for sand) used for the current simulation are summarized in Tables 1, 3, and 5, respectively, except that the density of the soil is set as 2,300 kg m^{-3}. The total computational time (or, wall-clock time) required to simulate the various physical processes in a 0.9 ms time interval following the initial explosive detonation of C4 in the cylindrical sand slab is 1.4 hours.

The temporal evolution of the velocity distribution associated with the damage of the 3D soil explosion to the Al plate obtained using the elastoplastic and elasto-viscoplastic constitutive models are shown in Figs 21 and 22, respectively. The physical processes associated with the C4 explosive detonation in soil are the same as those described in Section 6. It is noted that the apex (maximum) of the soil fragmentation impacts the bottom side of the Al plate at a time of 200 μs after the activation of the C4 charge. After this, the magnitude of velocity of the soil ejecta begins to decrease, as the momenta in the soil ejection is partially transmitted to the Al plate. The kinetic energy of the Al plate rapidly increases, causing the plate to deform elastically at first and then plastically later. It is seen that the deformation area on the target plate becomes more extensive with increasing time after the initial detonation. For example, a rather large deformation of the target plate (generated by the C4 explosive detonation) is clearly evident in Figs 21(f) and 22(f) corresponding to the predictions of plate deformation provided by the elastoplastic and elasto-viscoplastic constitutive models, respectively.

In order to investigate the dynamic behavior of the Al plate more quantitatively, the height of the deformation of the Al plate as a function of time is exhibited in Figs 23. At the initial time, the height of the plate deformation predicted using the elastoplastic constitutive model is a little larger than that obtained using the elasto-viscoplastic constitutive model. The height of the plate deformation is predicted to increase rapidly with increasing time. After 1000 μs, the velocity of the Al plate decreases gradually. The height and width of the plate deformation obtained using the elastoplastic model are generally smaller that those predicted using the elasto-viscoplastic model.

There are a number of possible reasons for this difference in the predictions provided by the two models. Firstly, the elastoplastic and elasto-viscoplastic models treat the granular material differently. The elasto-viscoplastic model treats the granular material as being disconnected when the material density is less than a critical value; otherwise, the material is considered to be a visco-plastic solid. This is different than the assumptions that underpin the elastoplastic model. Secondly,

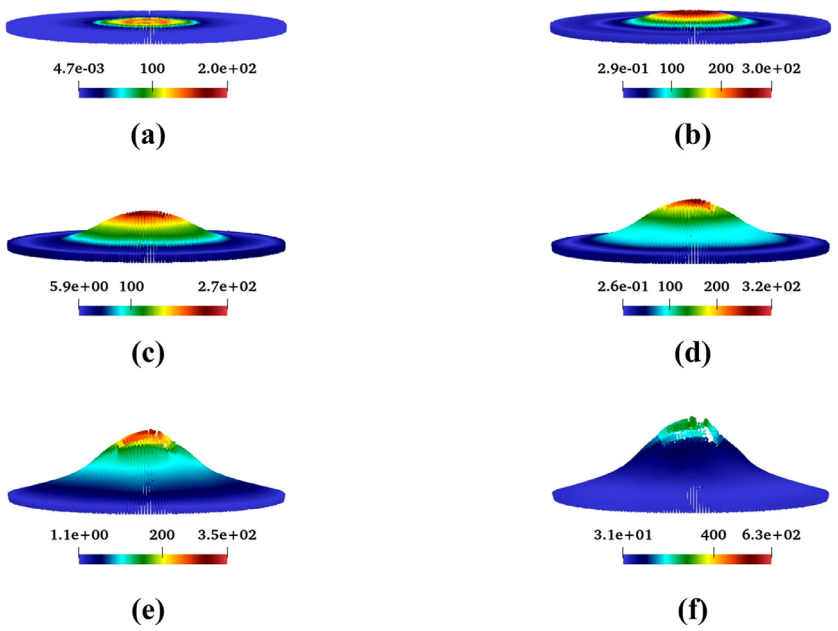

Fig. 21. The temporal evolution of the velocity distribution associated with the damage of the 3D soil explosion to the Al plate obtained using the elasto-plastic constitutive model at a time of (a) 300 μs, (b) 450 μs, (c) 700 μs, (d) 950 μs, (e) 1200 μs, and (f) 1400 μs after the initial C4 detonation.

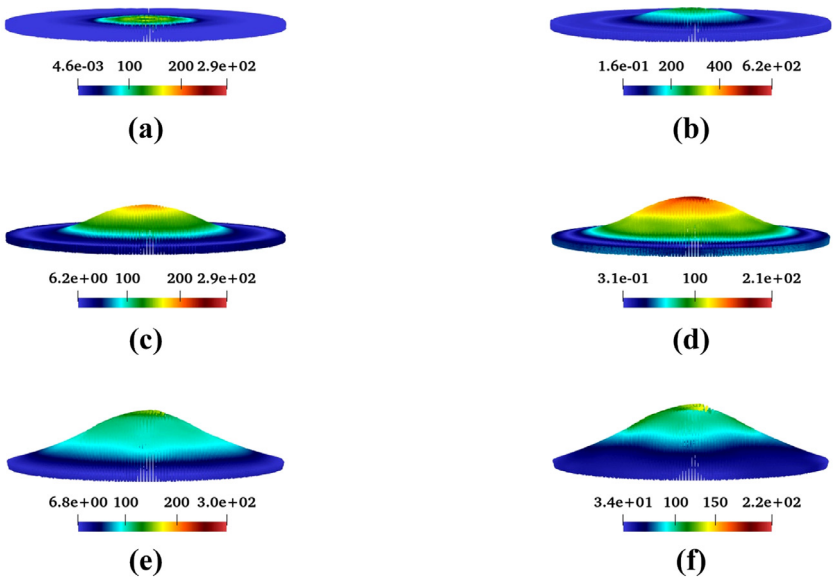

Fig. 22. The temporal evolution of the velocity distribution associated with the damage of the 3D soil explosion to the Al plate obtained using the elasto-viscoplastic constitutive model at a time of (a) 300 μs, (b) 450 μs, (c) 700 μs, (d) 950 μs, (e) 1200 μs, and (f) 1400 μ after the initial C4 detonation.

the friction coefficient of a static state μ_s and the maximum value of friction coefficient μ_2 used in the elasto-viscoplastic model for a dense granular flow may affect the numerical results. Owing to these two factors, the impulse of the impact of soil ejecta obtained from the elasto-viscoplastic model is expected to be larger than that obtained from the elastoplastic model. In addition, the plate deformations obtained from both of the elastoplastic and elasto-viscoplastic are compared to the experimental data from [45]. It can be observed that the agreement between numerical and experimental results is very good when the time is less than 1.15 ms. After 1.15 ms, the discrepancy becomes bigger. The maximum relative errors between the numerical deformations and the experimental deformations are less than 16%. The test case shown here suggests that our GPU-accelerated SPH methodology can be used to provide quantitative assessments of the damage to an Al plate incurred from an explosive detonation. The influence of different thickness of the target plate and different densities of the soil on the deformation of the Al plate will be investigated in a future effort using the proposed SPH methodology.

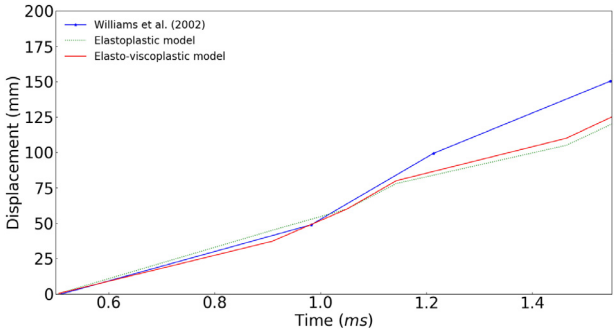

Fig. 23. Comparison of the height of plate deformation as a function of time obtained from the experiment [45] with the predicted height obtained from SPH using the elastoplastic and elasto-viscoplastic constitutive models.

8. Conclusions

In this paper, a SPH method is developed to simulate damage to Al plates caused by detonations of explosive devices in soil. Three types of materials are involved in this complex process, i.e., explosives, metals, and soils, which are modelled using the JWL EOS, the Grüneisen EOS and elastic-perfectly plastic model, and the elastoplastic and elasto-viscoplastic constitutive models, respectively. In the SPH method, the adaptive smoothing length and the treatment of interface with high density ratio are employed to tackle the complex multiphase and multiphysics phenomena. Furthermore, GPU acceleration is adopted to increase the computational efficiency of large-scale simulations with millions of particles.

Various components of the proposed method are thoroughly validated using several numerical examples, including explosive detonation, taylor bar impact, granular flow, and explosion in soil. Then the damage of Al plate caused by a detonation in soil is simulated. The following conclusions can be drawn from the simulation.

(1) The employed SPH method, combined with the various constitutive models, can provide numerical results well corroborated by experimental data. The maximum difference between numerically predicted and experimentally obtained deformations is 16%, which indicates that the method is reliable in modelling detonations and their interaction with Al plates.
(2) Two different constitutive models, i.e., the elastoplastic and the elasto-viscoplastic models, are used to simulate the dynamic behavior of soil materials. The simulations with these two models yield only slightly different results. Consequently, both of these two models are applicable, and either of them can be employed in future simulations.
(3) GPU acceleration is a powerful technique, which enables 3D simulations with high-resolution using easily available hardware. The GPU-accelerated SPH method can achieve more than 500 times of speed-up compared to serial CPU computing. This high efficiency allows using the SPH method to model practical applications.

Acknowlgedgments

The authors acknowledge the financial support provided by the National Natural Science Foundation of China (grant agreement no. 51909120).

References

[1] S.E. Rigby, S.D. Fay, S.D. Clarke, A. Tyas, J.J. Reay, J.A. Warren, M. Gant, I. Elgy, Measuring spatial pressure distribution from explosives buried in dry leighton buzzard sand, Int J Impact Eng 96 (2016) 89–104.
[2] S. Linforth, P. Tran, M. Rupasinghe, N.H. Nguyen, T. Ngo, M. Saleh, R. Odish, D. Shanmugam, Unsaturated soil blast: flying plate experiment and numerical investigations, Int J Impact Eng 125 (2019) 212–228.
[3] A.D. Resnyansky, S.A. Weckert, Experiments and constitutive modelling of sand ejecta impact, Journal of Dynamic Behavior of Materials 4 (4) (2018) 586–607.
[4] J.J. Monaghan, Smoothed particle hydrodynamics, Rep. Prog. Phys. 68 (8) (2005) 1703–1759.
[5] R.A. Gingold, J.J. Monaghan, Smoothed particle hydrodynamics: theory and application to non-spherical stars, Mon Not R Astron Soc 181 (3) (1977) 375–389.
[6] L.B. Lucy, A numerical approach to the testing of the fission hypothesis, Astron. J. (N. Y.) 82 (1977) 1013–1024.
[7] M.B. Liu, G.R. Liu, K.Y. Lam, Z. Zong, Smoothed particle hydrodynamics for numerical simulation of underwater explosion, Comput Mech 30 (2) (2003) 106–118.
[8] G.Y. Wang, G.R. Liu, Q. Peng, S. De, D.L. Feng, M.B. Liu, A 3D smoothed particle hydrodynamics method with reactive flow model for the simulation of ANFO, propellants, Explosives, Pyrotechnics 40 (4) (2015) 566–575.
[9] D.L. Feng, M.B. Liu, H.Q. Li, G.R. Liu, Smoothed particle hydrodynamics modeling of linear shaped charge with jet formation and penetration effects, Computers & Fluids 86 (2013) 77–85.
[10] H.F. Fan, S.F. Li, A peridynamics-SPH modeling and simulation of blast fragmentation of soil under buried explosive loads, Comput Methods Appl Mech Eng 318 (2017) 349–381.
[11] J.Y. Chen, F.S. Lien, Simulations for soil explosion and its effects on structures using SPH method, Int J Impact Eng 112 (2018) 41–51.
[12] J.Y. Chen, C. Peng, F.S. Lien, Simulations for three-dimensional landmine detonation using the SPH method, Int J Impact Eng 126 (2019) 40–49.

[13] J.Y. Chen, C. Peng, F.S. Lien, E. Yee, X.H. Zhao, Simulations for the explosion in a water-filled tube including cavitation using the SPH method, Computational Particle Mechanics 6 (4) (2019) 515–527.
[14] J.Y. Chen, F.S. Lien, C. Peng, E. Yee, GPU-Accelerated smoothed particle hydrodynamics modeling of granular flow, Powder Technol 359 (2020) 94–106.
[15] A. Mokos, B.D. Rogers, P. Stansby, J.M. Dominguez, Multi-phase SPH modelling of violent hydrodynamics on GPUs, Comput Phys Commun 196 (2015) 304–316.
[16] C. Peng, S. Wang, W. Wu, H.S. Yu, C. Wang, J.Y. Chen, LOQUAT: An open-source GPU-accelerated SPH solver for geotechnical modeling, Acta Geotech. 14 (5) (2019) 1269–1287.
[17] J.M. Domínguez, G. Fourtakas, C. Altomare, R.B. Canelas, A. Tafuni, O. García-Feal, I. Martínez-Estévez, A. Mokos, R. Vacondio, A.J. Crespo, B.D. Rogers, DualSPHysics: from fluid dynamics to multiphysics problems, Computational Particle Mechanics (2021) 1–29.
[18] L. Zhan, C. Peng, B.Y. Zhang, W. Wu, A stabilized TL–WC SPH approach with GPU acceleration for three-dimensional fluid–structure interaction, J Fluids Struct 86 (2019) 329–353.
[19] L. Zhan, C. Peng, B.Y. Zhang, W. Wu, Three-dimensional modeling of granular flow impact on rigid and deformable structures, Comput. Geotech. 112 (2019) 257–271.
[20] W. Dehnen, H. Aly, Improving convergence in smoothed particle hydrodynamics simulations without pairing instability, Mon Not R Astron Soc 425 (2) (2012) 1068–1082.
[21] M.B. Liu, G.R. Liu, K.Y. Lam, Z. Zong, Smoothed particle hydrodynamics for numerical simulation of underwater explosion, Comput Mech 30 (2) (2003) 106–118.
[22] J.J. Monaghan, An introduction to SPH, Comput Phys Commun 48 (1) (1988) 89–96.
[23] M.B. Liu, Z.L. Zhang, D.L. Feng, A density-adaptive SPH method with kernel gradient correction for modeling explosive welding, Comput Mech 60 (2017) 513–529.
[24] J.J. Monaghan, Simulating free surface flows with SPH, J Comput Phys 110 (2) (1994) 399–406.
[25] L. Libersky, A.G. Petschek, T.C. Carney, J.R. Hipp, F.A. Allahdadi, High strain lagrangian hydrodynamics: athree-dimensional SPH code for dynamic material response, J Comput Phys 109 (1) (1993) 67–75.
[26] S. Adami, X.Y. Hu, N.A. Adams, A generalized wall boundary condition for smoothed particle hydrodynamics, J Comput Phys 231 (21) (2012) 7057–7075.
[27] J.J. Monaghan, J.B. Kajtar, SPH Particle boundary forces for arbitrary boundaries, Comput Phys Commun 180 (10) (2009) 1811–1820.
[28] M. Ferrand, D.R. Laurence, B.D. Rogers, D. Violeau, C. Kassiotis, Unified semi-analytical wall boundary conditions for inviscid, laminar or turbulent flows in the meshless SPH method, Int J Numer Methods Fluids 71 (4) (2013) 446–472.
[29] E.L. Lee, C.M. Tarver, Phenomenological model of shock initiation in heterogeneous explosives, The Physics of Fluids 23 (12) (1980) 2362–2372.
[30] O. Heuzé, General form of the mie–Grüneisen equation of state, C.R. Mec. 340 (10) (2012) 679–687.
[31] P.W. Randles, L.D. Libersky, Smoothed particle hydrodynamics: some recent improvements and applications, Comput Methods Appl Mech Eng 139 (1–4) (1996) 375–408.
[32] H.H. Bui, R. Fukagawa, K. Sako, S. Ohno, Lagrangian meshfree particles method (SPH) for large deformation and failure flows of geomaterial using elastic–plastic soil constitutive model, Int J Numer Anal Methods Geomech 32 (12) (2008) 1537–1570.
[33] S. Dunatunga, K. Kamrin, Continuum modelling and simulation of granular flows through their many phases, J Fluid Mech 779 (2015) 483–513.
[34] J.M. Domínguez, A. Crespo, M. Gómez-Gesteira, J.C. Marongiu, Neighbour lists in smoothed particle hydrodynamics, Int J Numer Methods Fluids 67 (12) (2011) 2026–2042.
[35] J.Y. Chen, D.L. Feng, S.X. Deng, C. Peng, F.S. Lien, Gpu-accelerated smoothed particle hydrodynamics modeling of jet formation and penetration capability of shaped charges, J Fluids Struct 99 (2020) 103171.
[36] D. Dooge, R. Dwarampudi, G. Schaffner, A. Miller, R. Thyagarajan, M. Vunnam, V. Babu, Evolution of Occupant Survivability Simulation Framework Using FEM-SPH Coupling, in: Proceedings of the 2011 Ground Vehicle Systems Engineering and Technology Conference (GVSETS), 2011, pp. 1–14.
[37] R.L. Woodward, N.M. Burman, B.J. Baxter, An experimental and analytical study of the taylor impact test, Int J Impact Eng 15 (4) (1994) 407–416.
[38] D.L. Feng, M.B. Liu, H.Q. Li, G.R. Liu, Smoothed particle hydrodynamics modeling of linear shaped charge with jet formation and penetration effects, Computers & Fluids 86 (2013) 77–85.
[39] M.K.M. Nor, C.S. Ho, N. Ma'at, M.F. Kamarulzaman, Modelling shock waves in composite materials using generalised orthotropic pressure, Continuum Mech. Thermodyn. 32 (4) (2020) 1217–1229.
[40] G.R. Johnson, T.J. Holmquist, Evaluation of cylinder-impact test data for constitutive model constants, J Appl Phys 64 (8) (1988) 3901–3910.
[41] G. Sun, X.Y. Wang, W.L. Gao, J.C. Yang, X. Wang, Expansion fracture behavior of metallic cylindrical shell caused by explosive detonation, 2019, 267, 4, 042124.
[42] G. Lube, H.E. Huppert, R.S.J. Sparks, M.A. Hallworth, Axisymmetric collapses of granular columns, J Fluid Mech 508 (2004) 175–199.
[43] M. Grujicic, B. Pandurangan, B. Cheeseman, A computational analysis of detonation of buried mines, Multidiscipline Modeling in Materials and Structures 2 (2006) 363–388.
[44] D.M. Bergeron, R. Walker, C. Coffey, Detonation of 100-gram anti-personnel mine surrogate charges in sand, a test case for computer code validation, National Defence, Defence Research Establishment Suffield (1998).
[45] K. Williams, S.M. Clennan, R. Durocher, B. St-Jean, J. Tremblay, Validation of a loading model for simulating blast mine effects on armoured vehicles, 2002, 6, 35–44.